Motion of drops on inclined surfaces in the inertial regime

By BABURAJ A. PUTHENVEETTIL,† VIJAYA SENTHILKUMAR K., AND E. J. HOPFINGER‡

Department of Applied Mechanics, Indian Institute of Technology Madras, Chennai 600036, India.

(Received 13 April 2013)

We present experimental results of high Reynolds number motion of partially non-wetting liquid drops on inclined plane surfaces using (i) water on Fluoro-Alkyl Silane (FAS) coated glass and (ii) mercury on glass. The former surface is a high hysteresis (35°) surface while the latter a low hysteresis one (6°). The water drop experiments have been conducted for Capillary numbers $0.0003 < Ca < 0.0075$ and for Reynolds numbers based on drop diameter $137 < Re < 3142$. The range of Ca and Re for mercury on glass experiments are $0.0002 < Ca < 0.0023$ and $3037 < Re < 20069$. It is shown that when $Re \gg 10^3$ for water and $Re \gg 10$ for mercury, a boundary layer flow model accounts for the observed velocities. A general expression for the dimensionless velocity of the drop, covering the whole Re range, is derived, which scales with the modified Bond number (Bo_m). This expression shows that at low Re, $Ca \sim Bo_m$ and at large Re, $Ca\sqrt{Re} \sim Bo_m$. The dynamic contact angle (θ_d) variation scales, at least to first order, with Ca; the contact angle variation in water, corrected for the hysteresis, actually collapse on the low Re data of Le Grand *et al.* (2005). The receding contact angle variation of mercury has a slope very different from that in water, but the variation is practically linear with Ca. We compare our dynamic contact angle data to several models available in the literature. Most models can describe the data of Le Grand *et al.* (2005) for high viscosity silicon oil, but often need unexpected parameters to describe our water and mercury data. In particular, purely hydrodynamic description requires unphysically small values of slip length, while the molecular-kinetic model shows asymmetry between the wetting and dewetting, which is quite strong for mercury. The model by Shikhmurzaev (1993) is able to group the data for the three fluids around a single curve, thereby restoring a certain symmetry, by using two adjustable parameters that have reasonable values. At larger velocities, the mercury drops undergo a change at the rear from an oval to a corner shape when viewed from above; the corner transition occurs at a finite, receding contact angle. Water drops do not indicate such a clear transition from oval to corner shape. Instead, there appears to occur a direct transition from an oval shape to a rivulet.

1. Introduction

When drops move over surfaces, various regimes of motion occur based on the balance between the gravitational driving force, the contact line resistance and the viscous friction forces in the bulk. For the commonly occurring partially non-wetting fluid-surface

† Email address for correspondence: apbraj@iitm.ac.in
‡ Permanent address: LEGI/CNRS/UJF,Grenoble, France.

combinations, the lower resistance at the contact line and low kinematic viscosity often results in high Reynolds number (Re) motion of the drops. However, the Capillary number (Ca) can be low because common fluids have high surface tension. Such capillary and inertia dominated drop motion is of importance in spray coating, lithography, micro fluidics, drop condensation and in flow over hydrophobic coatings. In spite of the practical importance and the fundamental interest of this regime of drop motion, virtually no experimental results are available.

Onset of drop motion on an inclined plane occurs at a critical slope angle α_c at which the contact angle resistance is overcome by gravity. For a given drop volume V, α_c depends on the difference between the static advancing (θ_{sa}) and the static receding (θ_{sr}) contact angles, i.e. on the contact angle hysteresis $\theta_{sa} - \theta_{sr}$ (Bikerman 1950; Furmidge 1962; Dussan & Chow 1983; Dussan 1985). Once the motion is initiated, the drops move down the inclined surface at constant speed. The conditions at the contact line impose a resistance to the flow so that the velocity of an advancing liquid front is greater at the free surface than at the contact line, causing a rolling motion (Dussan & Davis 1974). By equating the driving gravitational potential energy - corrected for the losses at the contact line - to the predominant viscous dissipation in the wedge of fluid near the contact line, Ca, the dimensionless velocity of low Re viscous drops is obtained as,

$$Ca \sim Bo_m, \tag{1.1}$$

(Durbin 1988; Podgorski, Flesselles & Limat 2001; Kim, Lee & Kang 2002). Here, $Ca = \mu U/\sigma$ is the capillary number with U being the velocity of the drop, μ the dynamic viscosity and σ the surface tension of the fluid in air. The modified Bond number is,

$$Bo_m = Bo_\alpha - Bo_c, \tag{1.2}$$

with the Bond number defined as

$$Bo_\alpha = \rho V^{2/3} g \sin\,\alpha/\sigma, \tag{1.3}$$

where ρ is the density of the fluid, α the angle of inclination of the surface to the horizontal and g the acceleration due to gravity.

$$Bo_c = c_1 w(\cos\,\theta_{sr} - \cos\,\theta_{sa})/V^{1/3}, \tag{1.4}$$

where w is the width of the drop and c_1 a pre-factor of order one. $Re = Ud/\nu$ is the Reynolds number, with d being the undeformed drop diameter and ν the kinematic viscosity. The relation (1.1) is valid only when Re is small and when the variation of the dynamic contact angles (θ_d) are not appreciable from their static values; no general expression for the velocity of drops on inclines is available.

When the drop moves at appreciable velocities, the wetting or the dynamic advancing contact angles (θ_a) and the de-wetting or the dynamic receding contact angles (θ_r) change from their static values. Various models relating these dynamic contact angles (θ_d) with the dimensionless drop velocity, Ca have been proposed (Blake & Haynes 1969; Voinov 1976; de Gennes 1986; Cox 1986, 1998; Shikhmurzaev 1993); a recent review discusses some of these models (Bonn, Eggers, Indekeu, Meunier & Rolley 2009). All of these models are of the form

$$f(\theta_d, \theta_s) \sim Ca, \tag{1.5}$$

where θ_s denotes the static contact angle that is supposed to be equal to θ_{sa} or θ_{sr} in most models, based on whether we consider the advancing or the receding side. f is a transcendental function when the model is valid for all θ_d, but usually polynomial forms of f are obtained by truncating the series expansion of f for small θ_d. Le Grand *et al.*

(2005) compared the variations of θ_d, observed in the motion of drops of various silicon oils at $Re \ll 1$ and $Ca \leqslant 0.006$, with some of the models of dynamic contact angles. It was found that all the models agreed reasonably well with the trend of variation of θ_d with Ca, the Cox-Voinov hydrodynamic model (Cox 1986; Voinov 1976) performing the best, but needing smaller slip lengths λ with decreasing viscosity. Slip lengths are the microscopic lengths at which the hydrodynamic analysis has to be terminated to prevent singularities. However, studying the unsteady motion of the contact line in impact of drops on horizontal surfaces at $Re < 1000$, Bayer & Megaridis (2006) found that unphysically small λ are needed for the inertial version of the Cox model (Cox 1998). Similar need for unphysical λ in the viscous Cox-Voinov model (Cox 1986; Voinov 1976) were also found by Hayes & Ralston (1993) in water and glycerol on PET, at $Re < 27$. At the same time, Le Grand *et al.* (2005) found that except for the Cox-Voinov model (Voinov 1976; Cox 1986), all the other models need an asymmetry in the variation of $f(\theta_d, \theta_s)$ with Ca for the receding and advancing sides to fit the data. Since these models are local and do not distinguish between θ_a and θ_r, the change of $f(\theta_d, \theta_s)$ with Ca is expected to be the same for the receding and advancing sides when $Ca \to 0$, at least in the initial version of these theories.

With increasing speeds of motion, drops also undergo a shape transition at the rear. Studies by Podgorski *et al.* (2001) with silicon oil drops showed that the drops first develop a corner and then a cusp at the rear at two critical speeds. The corner formation was considered to be a forced wetting transition and was proposed to occur at zero contact angle. Ben Amar *et al.* (2003) proposed a model in which such a corner forms at zero contact angle as a saddle point, but this model neglected the dissipation in the bulk of the corner. Considering this dissipation, Limat & Stone (2004) then found theoretically that a corner needs a conical shape of the interface with a non zero contact angle. In agreement with this theory, Le Grand *et al.* (2005) found by studying silicon oil drops of a wide range of viscosities (10cP-1000cP) that the corner transition takes place at a non-zero receding contact angle, contrary to the assumptions of Blake & Ruschak (1979) and the hypothesis of Podgorski *et al.* (2001). The self similar velocity field in such a corner and its evolution with Ca has then been studied by Snoeijer *et al.* (2007, 2005), even though no criterion for the formation of the corner is available. Such a forced wetting transition at a non-zero critical receding contact angle was predicted only by the de Gennes model(de Gennes 1986); the Cox-Voinov model predicted a forced wetting transition at $\theta_r = 0$. However, the de Gennes model deviated from the experiments of Le Grand *et al.* (2005) near the forced wetting transition.

The above-mentioned studies were conducted with viscous and fairly wetting drops, i.e. small θ_d conditions at small Re and Ca. There is no available information on the velocity and dynamic contact angle variation of partially non-wetting drops with large θ_d as a function of the fluid properties and the inclination angles at high Re. However, the complete non-wetting case have been studied by Mahadevan & Pomeau (1999) and Richard & Quéré (1999). Since the local Re can be small at the resolution of the contact angle measurement, even if the Re of the drop is large, the issue of whether θ_d depends on inertia, as has been proposed by Cox (1986), is still not clear. It is therefore of interest to conduct experiments with drops of large θ_d and Re, but keeping Ca small. We achieve such a regime by using mercury drops ($\theta_s \approx 140^\circ$) on a glass surface and water drops on Fluoro Alkyl Silane (FAS) coated glass ($\theta_s \approx 90^\circ$). The water drops are made to move on an inclined FAS coated glass plate with a velocity in the range of $0.025\text{ms}^{-1} < U < 0.603$ ms^{-1} for an inclination angle range of $26^\circ < \alpha < 62^\circ$. For safety reasons, the mercury drop was placed inside a sealed glass cylinder rotating about a horizontal axis so that the drop was frozen relative to the observer. The range of velocities for the mercury drops

are $0.07\ \mathrm{ms}^{-1} < U < 0.72\ \mathrm{ms}^{-1}$; Re as large as 2×10^4 are achieved, while Ca are small ($Ca < 0.0075$).

Drops offer an advantage in exploring the inertial effect on contact angles since straight contact lines tend to be unstable resulting in a saw tooth pattern (Blake & Ruschak 1979) or fingering (Jerrett & de Bruyn 1992) at large Re. For a film on an inclined plate at a given Ca, Re, slip length λ and α, all the wavelengths larger than a critical wavelength λ_c are unstable(Lopez, Bankoff & Miksis 1996; Lopez, Miksis & Bankoff 1997). The advantage of using drops to study contact angles is that small drops cut off the large wavelengths due to their finite size so that a drop is more stable than a film at the same Ca and Re. A gravitationally driven film is unstable to perturbations of wavelength $\lambda_p \geqslant 2\pi l/0.9$ where $l = (H\sigma/\rho g)^{1/3}$ is the length scale given by a gravity surface-tension balance, with H being the film thickness (Troian, Herbolzheimer, Safran & Joanny 1989). A film of the height of our drops will be unstable for lengths larger than 17mm for mercury and 15.4 mm for water. Bertozzi & Brenner (1997) have shown that fingers will form on advancing films if $\theta_d < \tan\alpha \ln(H/\lambda)$. This condition gives $\alpha > 8.3^\circ$ for water and $\alpha > 11.3^\circ$ for mercury, the corresponding velocities will be quite small compared to the values that we encounter in our experiments with our drops. Earlier studies (Blake, Bracke & Shikhmurzaev 1999) have attempted experiments with straight contact line geometries by plunging tape and falling curtain experiments, but with very viscous liquids, and have found saw tooth configuration and air entrainment at the advancing contact line at Re of around 47. On the contrary, since the curved advancing contacting line in our case is with a radius $R_b \sim l_c$, where $l_c = \sqrt{\sigma/\rho g}$ is the capillary length, the contact line is stable and we are able to reach $Re < 20069$ for the first time. In addition to the large Re, another novelty in the present study lies in the large values of θ_d due to which comparison with the non-truncated, cosine forms of the popular dynamic contact models are conducted.

The paper is organised as follows. The experimental setup and techniques are presented in § 2. In § 3, we derive simple expressions for the velocity of the drops from global energy balance, neglecting θ_d variations. In § 4, we compare the predictions of dynamic contact angles by various models with our measurements. The observations of the shape change of the drop with velocity, presented in § 5, bring out the difference between the low hysteresis mercury drops and the high hysteresis water drops. Conclusions and further discussions are presented in § 6. The experiments presented in this paper were conducted by VSK. The boundary layer model was proposed by BAP, while the general dimensionless form for the velocity was found out by EJH and BAP. The comparison with various contact angle models were conducted by BAP and EJH. The comparison with the Shikmurzaev's model was done by BAP. The paper and the replies to the Referees were written by BAP and EJH.

2. Experimental conditions

2.1. *Setup*

The experimental set-up for studying the motion of water drops is shown in figure 1. A glass plate, coated with Fluoro Alkyl Silane (FAS), of dimensions 55×10 cm was fixed in an inclined position with one end supported by a thread of adjustable length so as to allow changes in the inclination angle of the plate. To coat the glass plate with FAS, it was first wetted with water, rubbed with fine cerium oxide to create a nascent surface and then cleaned thoroughly. A solution of FAS, alcohol and an acid catalyst was then applied thoroughly on the glass surface. The coated surface was then dried and then

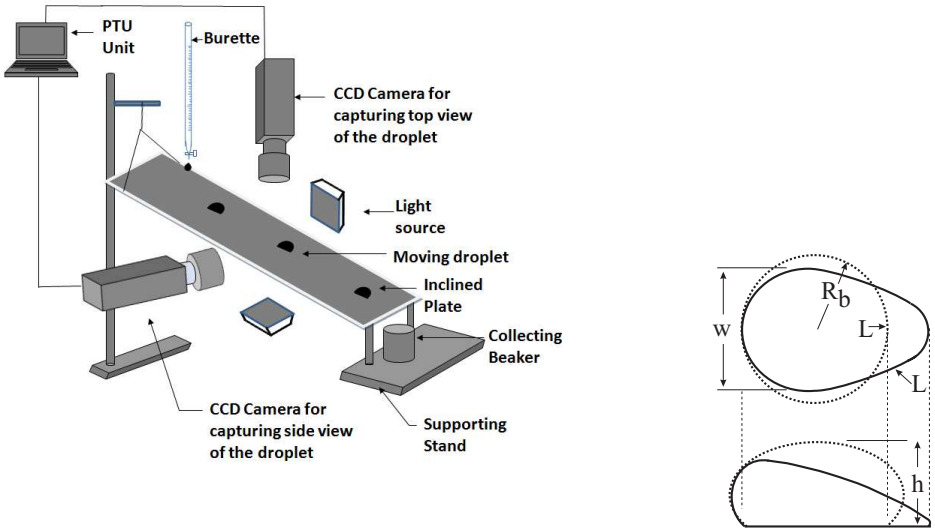

FIGURE 1. (a) Schematic of the inclined plate setup for water drops. (b) Schematic of the drop geometry. The dotted line in the top view shows the equivalent circular base of the drop which has the same base perimeter L as the actual drop.

polished with soft, glass polishing cloth and allowed to cure at room temperature for 12 hours. The FAS coated glass plate was thoroughly cleaned with acetone, propanol and distilled water to make it dust free and homogeneous. The mono-layer of Silane molecules binds to the glass surface, thereby changing the surface energy, and hence the contact angles to make the glass surface partially non-wetting. θ_{sa} and θ_{sr} for water drops were measured to be 109° and 73° respectively. Small non-uniformities in the coverage of the mono-layer on the glass surface results in chemical inhomogeneities, causing most of the contact angle hysteresis. Since the coating is at a molecular scale, it does not contribute to the physical roughness of the underlying glass substrate at a macroscopic level (Hozumi, Ushiyama, Sugimura & Takai 1999). The glass could have roughness at the nanometer level, but could be considered as smooth at the macroscopic level. Water drops were issued continuously from a burette onto the inclined glass plate. The mass of the drop was $m = 52.7 \pm 0.5$ mg ($d = 4.7 \pm 0.015$ mm) when the water level in the burette was maintained above the 15 cc mark. After a few millimetres of initial adjustment, the water drop slides with a constant velocity as a result of the balance between the viscous, contact line and gravitational forces.

For safety reasons, the mercury drops were placed inside a horizontal tube made of float glass and sealed; rotation of the tube about a horizontal axis creates equivalent conditions as in the case of an inclined plate. The setup consists of a horizontally rotating glass tube of radius 7.5 cm, fixed co-axially to the shaft of a variable speed electric motor as shown in figure 2. The mercury drop, of undeformed diameter $d = 3.15 \pm 0.01$ mm, having a mass of $m = 220 \pm 2$ mg, is placed inside the tube, sealed and then the tube is rotated at various rotation rates less than 3619 RPM. For each rotation speed, the drop moves along the inner surface of the tube and becomes stationary when a balance among viscous, gravitational and contact line forces is achieved. Since the drop size is small compared to the tube radius, the conditions are analogous to the steady motion of

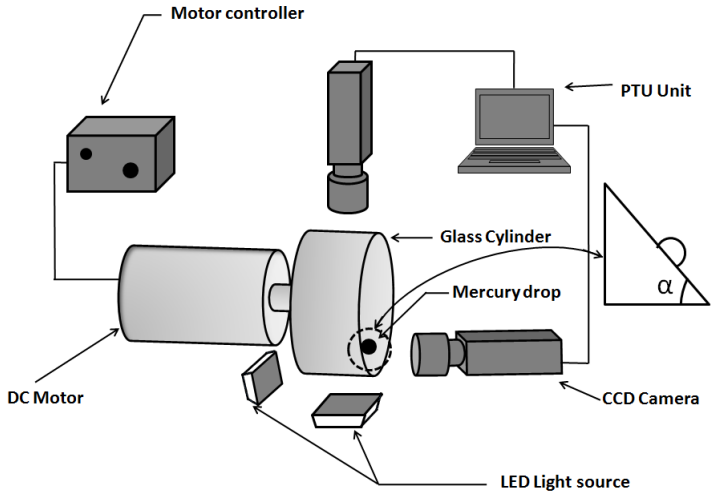

FIGURE 2. Schematic of the rotating glass tube setup for mercury drops.

a drop on an inclined plate. There are no centrifugal effects since the drop is stationary in the laboratory frame of reference. The mercury experiments can be considered to be conducted on a surface that is smooth on a macroscopic scale since float glass has no physical roughness at scales larger than nano meters (Gupta, Inniss, Kurkjian & Zhong 2000). In addition, we thoroughly clean the glass surface with acetone, propanol and distilled water before each experiment thereby reducing the chemical inhomogeneities. The small contact angle hysteresis ($\theta_{sa} - \theta_{sr} = 6^\circ$) observed on this surface (see table 1) shows the smooth nature of the surface.

Two CCD cameras (Imager Pro HS, La Vision, GMBH) were used to visualise the top and side views of both the drops simultaneously at 25 fps with two LED light sources of intensity 1500 lumens, as shown in figure 1. The properties and dimensions of the mercury and water drops used in the experiments are listed in table 1.

2.2. *Diagnostics and Data analysis*

The three main measurements in the experiments are:

(a) the inclination angles of the solid surfaces from the horizontal,
(b) the velocity of the drops,
(c) the dynamic contact angles of the drops.

The inclination angles in the experiments with water drops are obtained by measuring the angles between the line segments fitted tangential to the inclined plate and parallel to the horizontal axis in the side view images of drops. The range of inclination angles used in the experiments was $26^\circ < \alpha < 62^\circ$. In the case of mercury drops, the drop will come to rest at a specific position for a particular rotation rate of the glass tube. The equivalent inclination angle α is measured from the side view of the drop by fixing a tangent to the rim of the glass tube at the location of the drop. Since at larger velocities, the mercury drops were not completely stationary, the value of the angle was determined at each position by taking an average over a few frames. The range of inclination angles were $5.5^\circ < \alpha < 14.3^\circ$. The errors in the inclination angles were less than 1.5°.

Parameters and fluid properties at 25°C	Mercury-Glass	Water-FAS coated glass
Surface tension σ (Nm^{-1})	485×10^{-3}	72×10^{-3}
Viscosity μ (Pa.s)	1.53×10^{-3}	0.891×10^{-3}
Density ρ ($\mathrm{kg\ m}^{-3}$)	13533.6	997
Capillary length l_c (mm)	1.9	2.7
Drop mass m (mg)	220 ± 2	52.7 ± 0.5
Drop diameter d (mm)	3.15 ± 0.01	4.7 ± 0.015
Base perimeter L (mm)	11	18.8
Base radius R_b (mm)	2.5	3
Base width w (mm)	4	3.3
$\ln(R_b/\lambda)$	13	13
Static advancing angle θ°_{sa}	150.63	108.8
Static receding angle θ°_{sr}	144.57	73.4
Critical slope angle α°_{c}	2.8	25
Ca	0.23×10^{-3} - 2.3×10^{-3}	0.3×10^{-3} - 7.5×10^{-3}
Re	2049 - 20069	137 - 3142
Critical Bond number $Bo_{\alpha c}$	0.085	0.81

TABLE 1. Fluid properties, contact angles and the range of parameters in the experiments. The Bond number $Bo_\alpha = \rho V^{2/3} g \sin\alpha/\sigma$, the Reynolds number $Re = Ud/\nu$, where $d = 2(3V/4\pi)^{1/3}$, w is the width of the drop base and R_b is the mean drop base radius, defined as $R_b = L/2\pi$, where L is the drop base perimeter. λ is the slip length. The values of w and R_b are the mean values for $0.0014 < Ca < 0.0043$ for water and for $0.0011 < Ca < 0.0025$ for mercury. The properties of the fluids used are taken from Batchelor (1969).

The velocity of the sliding water drop is obtained from the displacement of the drop in subsequent frames in top view images, after taking an average from several frames. The range of variation of the velocity at each inclination angle was less than 5%. The velocity of the mercury drops relative to the glass surface is the same as the velocity of the glass surface since the mercury drops are, in the mean, stationary with respect to the camera. The velocity of the glass surface is calculated from the measured rotation rate of the glass tube. The rotation rate of the glass tube was read out from the motor controller and independently measured with a digital tachometer with an accuracy of ±2 rpm.

The dynamic contact angles for water and mercury drops are measured between the tangents fitted to the solid-liquid and the liquid-air interfaces in the zoomed side views in the image processing software Image J™. The contact angles reported are averages from a minimum of four measurements at each velocity. The range of variation of θ_d at each velocity is about 3°. The side view images are acquired at 25 frames per second with a resolution of 0.1mm per pixel. It is shown in Appendix A that an increase in resolution of the images does not change the contact angles appreciably from the measured values. Due to the curved nature of the contact line, the angle that the contact line makes with the direction of drop motion changes along the periphery. Owing to this, the velocity of the contact line perpendicular to itself is different along the periphery; the contact angles are also hence different along the periphery of the drop (Prabhala, Panchagnula & Vedantam 2012; Rio, Daerr, Andreotti & Limat 2005). However, at the front and the back of the drop, the contact line moves perpendicular to itself and the contact line velocity is equal to the drop velocity, till a corner/cusp forms. We hence measure the contact angles and the velocities at the front and the back of the drop. The influence of the variation of contact angles along the periphery on the velocities and the contact

angles that we measure is negligible since there is negligible flow along the periphery of the drop; all the flow at the front and the back are in the vertical plane.

3. Drop Velocities

3.1. *Theoretical Background*

For a given α, there exists a critical drop volume V_c at which impending drop motion is observed. Conversely, for a given drop volume V, there exists a critical slope angle α_c for impending motion. At this critical slope angle, the gravitational force,

$$F_g = \rho V g \sin\,\alpha_c, \tag{3.1}$$

is in balance with the local triple line pinning force,

$$F_{cl} = c_1 \sigma w(\cos\,\theta_{sr} - \cos\,\theta_{sa}), \tag{3.2}$$

where c_1 is a coefficient of order unity, determined from experiments. The critical slope angle resulting from $F_g = F_{cl}$ is then,

$$\sin\alpha_c = \frac{c_1 \sigma w(\cos\,\theta_{sr} - \cos\,\theta_{sa})}{\rho g V}. \tag{3.3}$$

Taking $w = c_2 V^{1/3}$, (3.3) can be written in terms of a critical Bond number in the form,

$$Bo_c = \frac{\rho g V^{2/3} \sin\,\alpha_c}{\sigma} = c_1 c_2(\cos\,\theta_{sr} - \cos\,\theta_{sa}). \tag{3.4}$$

The water drops have a volume $V = 0.0529$ cm^3 and their base width is $w \approx 3.3$mm (see table 1), which gives $c_2 \approx 0.87$. Since the measured critical slope angle at impending motion is $\alpha_c \approx 25^\circ$, we get $c_1 \approx 1.5$ from (3.3). Similarly, we obtain $c_2 \approx 1.57$ and $c_1 \approx 0.97$ for mercury drops, since their volume is $V = 0.01625$ cm^3, the base width is $w \approx 4$mm and the measured critical slope angle is $\alpha_c \approx 2.8^\circ$. At impending motion the shape of the mercury and the water drops are very different so that c_2 is expected to be different. Consequently, c_1 will also be different for the mercury and water drops. The high hysteresis of water causes the elongation of the drop resulting in $c_1 \neq 1$, contrary to the result of Dussan & Chow (1983). We point out here that α_c is very sensitive to any outside perturbations like surface conditions at the microscopic scale, the way the drop is placed, stick slip behaviour etc.; the angle could not hence be determined with high accuracy. For small contact angle hysteresis ($< 10^\circ$) the expression of Bo_c given by Dussan (1985) is,

$$Bo_c = \left(\frac{24}{\pi}\right)^{1/3} \frac{(\cos\,\theta_{sr} - \cos\,\theta_{sa})(1 + \cos\,\theta_{sa})^{1/2}}{(2 + \cos\,\theta_{sa})^{1/3}(1 - \cos\,\theta_{sa})^{1/6}}. \tag{3.5}$$

This expression gives $\alpha_c \approx 1.13^\circ$ for mercury, a value considerably less than the experimental value. Mercury drops do have a small contact angle hysteresis but the contact angles are large, larger than 90°, and it is not clear whether (3.5) still applies in this case. In all further calculations we hence use the values of $c_1 = 1.5$ for water and $c_1 = 1$ for mercury obtained from experiments as described above.

Drops larger than V_c, or drops on slopes larger than α_c, will start moving resulting in retarding forces due to the action of viscosity. For low Re drops these retarding forces are the force from the shear stress due to the Stokes wedge flow,

$$F_w = 4c_3 \mu c(\theta_e) L U \ln(R_b/\lambda), \tag{3.6}$$

and the force from the shear stress associated with the bulk motion,

$$F_b = c_4 \mu U (V_b/h^2). \tag{3.7}$$

In (3.6) and (3.7), R_b is the base radius of the drop, the base perimeter of the drop $L = 2\pi R_b$, h is the drop height and c_3 and c_4 are constants of order unity. The base volume $V_b = \pi R_b^2 h$ and λ is the microscopic cut-off length scale (slip length of a few molecular lengths) where the continuum approximation fails; it is typically of the order of 10 nm. In (3.6),

$$c(\theta_e) = \frac{\sin^2 \theta_e}{2\theta_e - \sin^2 \theta_e}, \tag{3.8}$$

is obtained by integrating the viscous dissipation per unit volume, calculated from the velocity field of Huh & Scriven (1971), in the wedge near the contact line (Kim, Lee & Kang 2002). Equation (3.8) is a function of the mean static contact angle $\theta_e = (\theta_{sa} + \theta_{sr})/2$. The justification for using the solution of Huh & Scriven (1971) in estimating F_w is given in Appendix B.

Steady motion of the drop then requires that,

$$F_g - F_{cl} = F_w + F_b, \tag{3.9}$$

implying,

$$U = \frac{\rho V g \sin \alpha - c_1 \sigma w (\cos \theta_{sr} - \cos \theta_{sa})}{\mu [c_4 (V_b/h^2) + 4 c_3 L c(\theta_e) \ln(R_b/\lambda)]}, \tag{3.10}$$

(Kim, Lee & Kang 2002). The ratio of wedge to bulk friction forces F_w/F_b is

$$\frac{F_w}{F_b} \approx \frac{c_3 8 c(\theta_e) \ln(R_b/\lambda)}{c_4 R_b/h}. \tag{3.11}$$

When $l_c > d/2$, R_b/h in (3.11) is approximately equal to 1 since the drop will be approximately hemispherical. Since c_3 and c_4 are of order one and $8c(\theta_e)\ln(R_b/\lambda) \gg 1$, as per (3.11), wedge dissipation dominates over bulk dissipation when $l_c > d/2$. As we show later in figure 4, wedge dissipation dominates over bulk dissipation in our experiments since $l_c > d/2$. As will be seen below, (3.10) is however not valid for drop motion at large Re.

3.2. *Measured drop velocities*

The measured velocities of water and mercury drops are shown in figure 3. The error bars shown in the figure for water drops show the range of variation of the velocity at any inclination angle. For the inclination angle range of $26^\circ \leqslant \alpha \leqslant 50^\circ$ ($U < 0.37$ ms^{-1}), Re of water drops are in the range $130 \leqslant Re \leqslant 1910$. Beyond $\alpha \sim 50^\circ$ rivulets form so that the analysis does not hold due to the large deviation of the drop geometry from the values used in (3.10). In the figure, the water drop velocities are compared with equation (3.10) using $c_1 = 1.5$ obtained from the condition of impending motion (3.3). Even though the velocities predicted by (3.10) are slightly higher than the measured values there is a good agreement of (3.10) with the trend of measured velocities when $c_3 = 1.6$ and $c_4 = 1$. In the relatively large Re regime of water drops in figure 3, we would expect the viscous dissipation to be more and more concentrated in a thin boundary layer near the wall so that (3.10) is no longer valid. As we show below, the above behaviour of water drops is understandable for the present range of Re because the boundary layer dissipation starts to dominate only at $Re \gg 10^3$ for water drops.

The velocities of mercury drops, which have a range of $3038 \leqslant Re \leqslant 9673$ in figure 3, are more than an order of magnitude lower than that given by (3.10) when the pre-factor

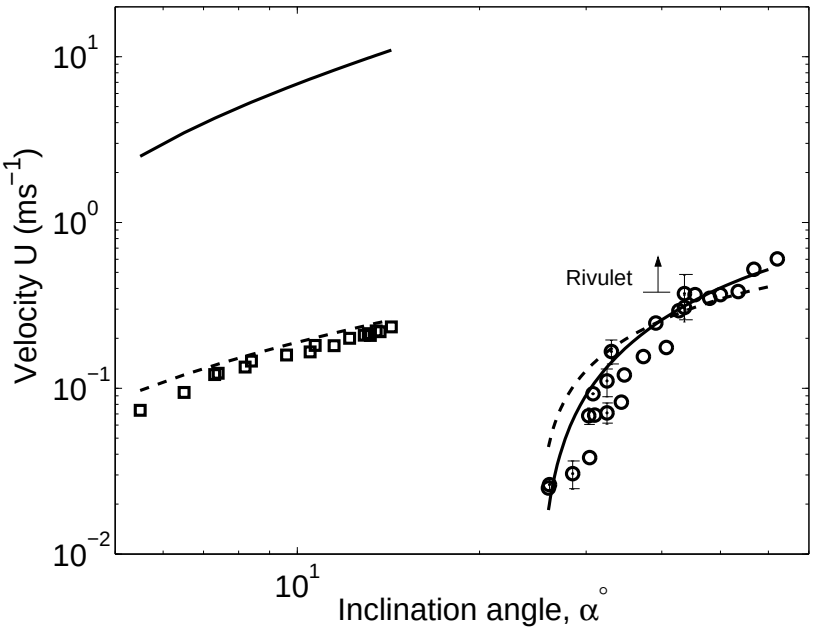

FIGURE 3. Drop velocities as a function of slope angle α in degrees; ○, water; □, mercury; —, equation (3.10); −−, equation (3.16). The pre-factors used are $c_1 = 1.5$ for water and $c_1 = 1$ for mercury. $c_3 = 1.6$, $c_4 = 1$ and $c_5 = 1.8$ for both fluids.

$c_1 = 1$ is used. As described in § 3.1, this value of c_1 is obtained from the impending motion condition (3.3), c_3 and c_4 being the same as in the case of water drops. We now show that the velocities of mercury drops are in good agreement with a boundary layer model that we propose below.

3.3. *Boundary layer model*

At large Re, there will be boundary layers inside the drop near the solid surface; the dissipation inside these boundary layers will dominate over the dissipation in the bulk of the drop. Let the thickness of the boundary layer near the solid surface be $\delta \sim \sqrt{\nu t}$. Taking $t \sim R_b/U$ as the characteristic time scale, we get,

$$\delta \sim \sqrt{\nu R_b/U}. \tag{3.12}$$

The dimensionless boundary layer thickness calculated from (3.12) for the present experimental range is $0.06 < \delta/d < 0.015$ for water drops and $0.01 < \delta/d < 0.005$ for mercury. δ is hence about two orders of magnitude smaller than the drop size for the range of Re in the present study. The viscous force is now $F_{bl} = V_{bl}\mu\partial^2 U/\partial z^2$, where the boundary layer volume $V_{bl} \approx \pi R_b^2 \delta$ and z is the co-ordinate direction normal to the surface. Using $\partial U^2/\partial z^2 \approx U/\delta^2$, we get

$$F_{bl} = c_5 \mu \pi R_b U \sqrt{Re_b}, \tag{3.13}$$

where $Re_b = UR_b/\nu$ is the Reynolds number based on R_b. In an inertial regime, the steady force balance is, $F_g = F_{cl} + F_{bl} + F_w$, which results in,

$$\rho V g \sin\alpha - c_1 \sigma w(\cos\theta_{sr} - \cos\theta_{sa}) = c_5 \mu \pi R_b U \sqrt{Re_b}\,(1+\zeta)\,, \tag{3.14}$$

where

$$\zeta = \frac{c_3 8 c(\theta_e) \ln(R_b/\lambda)}{c_5 \sqrt{Re_b}}. \tag{3.15}$$

$\zeta \ll 1$ when $F_{bl} \gg F_w$, or when Re_b is appreciable. The expression for the velocity of the drop obtained by neglecting F_w when $\zeta \ll 1$ is then,

$$U = \frac{1}{R_b} \left(\frac{\rho V g \sin\alpha - c_1 \sigma w (\cos\theta_{sr} - \cos\theta_{sa})}{c_5 \rho \pi \nu^{1/2}} \right)^{2/3}. \tag{3.16}$$

Using the values of pre-factors in figure 3 and the value of $c(\theta_e)$ from (3.8) in (3.15), we get that $\zeta \sim 1$ for mercury drops when $Re \approx 24$; (3.16) is hence valid when $Re \gg 10$ for mercury. It is seen in figure 3 that (3.16) agrees well with the mercury data in our experiments which have $Re > 3038$. Since Re of mercury drops is much larger than 24 in the present experiments, mercury drops move in a predominantly inertial regime where the velocity is decided by a balance of the sum of boundary layer dissipation and contact line dissipation with the gravitational potential energy changes.

Similarly, $\zeta \sim 1$ for water when $Re \sim 1280$ from (3.15) and (3.8); equation (3.16) is hence valid for water when $Re \gg 10^3$. Inertial effects are likely to be dominant in water when $Re \gg 10^3$. When $Re \ll 10^3$, equation (3.14) leads to (3.10), with which the measured velocities in water approximately match for $Re < 2 \times 10^3$, as shown in figure 3. For water drops $626 < Re < 1910$ ($0.12\ \mathrm{ms}^{-1} < U < 0.37\ \mathrm{ms}^{-1}$) when $35^\circ < \alpha < 50^\circ$. In this range both equations (3.10) and (3.16), seems to match the experimental trends reasonably well, even though both curves predict higher velocities than experiments. It appears that for $35^\circ < \alpha < 50^\circ$ the water drops are in a transition regime between an inertial regime where the boundary layer dissipation dominates and a regime where the wedge dissipation dominates. In such a transition regime both equations (3.10) and (3.16) could over predict the velocities since each of these neglects boundary layer dissipation and wedge dissipation respectively; both these dissipations could be important in the transition regime. More details about the range of validity of (3.10) and (3.16) based on dissipation estimates are given in § 3.4. Figure 3 also shows that for water drops the velocities predicted by (3.16), for $\alpha > 50^\circ$, tend to be lower than the measured velocities, the deviation increasing with larger Re. This behaviour would imply that, at larger velocities, the actual dissipation is not as much as estimated from the boundary layer model. We now try to understand these behaviours of water and mercury drops by evaluating the variation of different dissipation rates with Re.

3.4. *Variation of the dissipation rates*

The various dissipation terms in the energy balance $\Phi_g - \Phi_{cl} = \Phi_w + \Phi_b + \Phi_{bl}$ can be calculated from equations (3.1), (3.2), (3.6) (3.7) and (3.13) noting that $\Phi_i = UF_i$. To understand the contribution of each of these terms we plot the individual dissipation terms, normalised by Φ_g, as a function of Re in figure 4. Φ_b is negligible for both the fluids and is negligible in (3.10). We depict Φ_b in figure 4 only to show its relative magnitude with other dissipations. From the normalised dissipation rates of the mercury drops plotted in figure 4(a), it is clear that Φ_{cl} is of the order of Φ_g due to the high surface tension, even though the hysteresis of mercury drops is low. The boundary layer dissipation rate Φ_{bl} is much larger than Φ_w and Φ_b in the whole Re range. The predominant balance obtained is thus $\Phi_g - \Phi_{cl} \approx \Phi_{bl}$ resulting in good agreement of the mercury drop velocities with the boundary layer model (3.16).

The variation of the different normalised dissipation terms for water drops are shown in figure 4(b). The contact line dissipation Φ_{cl} is of the order of the rate of potential

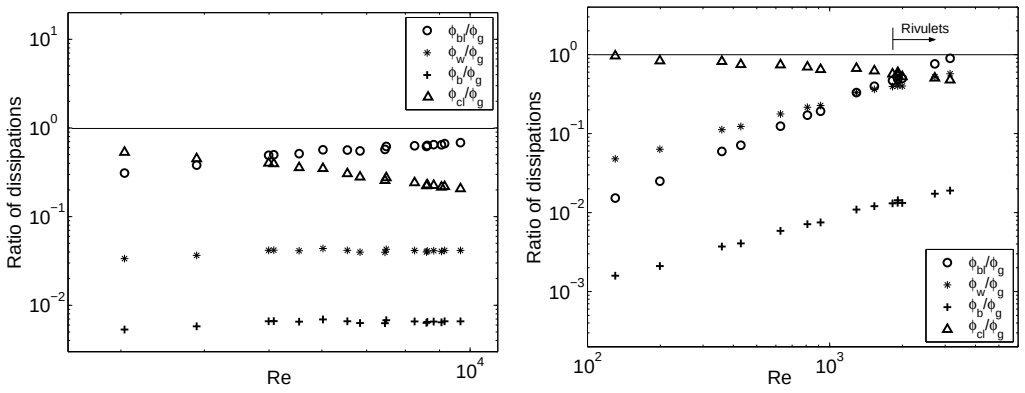

FIGURE 4. Variation of energy dissipation rates, normalised by Φ_g, with Re for (a), mercury and (b), water. The pre-factors used are $c_1 = 1.5$ for water and $c_1 = 1$ for mercury. $c_3 = 1.6$, $c_4 = 1$ and $c_5 = 1.8$.

energy loss Φ_g and hence plays a major role in determining the velocity of the drop. Even though the surface tension of water drops is an order of magnitude lower than that in mercury, Φ_{cl} is dominant due to the high contact angle hysteresis. The importance of contact line dissipation and wedge dissipation up to high Re explains the reasonably good agreement of the water drop velocities with equation (3.10). It is seen that the boundary layer dissipation $\Phi_{bl} \sim \Phi_w$ when $Re \sim 1000$, in agreement with the conclusions arrived in § 3.3. At $Re \sim 1000$ there is a cross over from a wedge dissipation dominated regime to a boundary layer dominated regime. However it is only when $Re \ll 10^3$ that the predominant balance becomes $\Phi_g - \Phi_{cl} \approx \Phi_w$ and only when $Re \gg 10^3$ that the predominant balance is $\Phi_g - \Phi_{cl} \approx \Phi_{bl}$. For $Re \sim 10^3$, as is in the major part of the water data, $\Phi_g - \Phi_{cl} \approx \Phi_{bl} + \Phi_w$. Equations (3.10) and (3.16) neglect boundary layer dissipation and wedge dissipation respectively, neither of which are negligible in the range of Re for the water drops in the present experiments. This could also be the reason for equations (3.10) and (3.16) to go slightly above the experimental data, for $Re < 1000$ in figure 3.

3.5. *Dimensionless velocities in the inertial regime*

When (3.14) is written in dimensionless terms, we get,

$$\frac{We_b}{\sqrt{Re_b}}\,(1+\zeta) = K_1 Bo_m, \tag{3.17}$$

a general scaling relation valid for the whole Re range. Here, $K_1 = V^{1/3}/(c_5\pi R_b)$, $We_b = \rho U^2 R_b/\sigma$ is the Weber number, $Bo_m = Bo_\alpha - Bo_c$ is the modified Bond number, $Bo_\alpha = \rho V^{2/3} g \sin\alpha/\sigma$ and $Bo_c = c_1 w(\cos\theta_{sr} - \cos\theta_{sa})/V^{1/3}$. When boundary layer dissipation dominates over wedge dissipation, $\zeta \ll 1$, (3.17) reduces to the dimensionless form of (3.16),

$$\frac{We_b}{\sqrt{Re_b}} = Ca\sqrt{Re_b} = K_1 Bo_m. \tag{3.18}$$

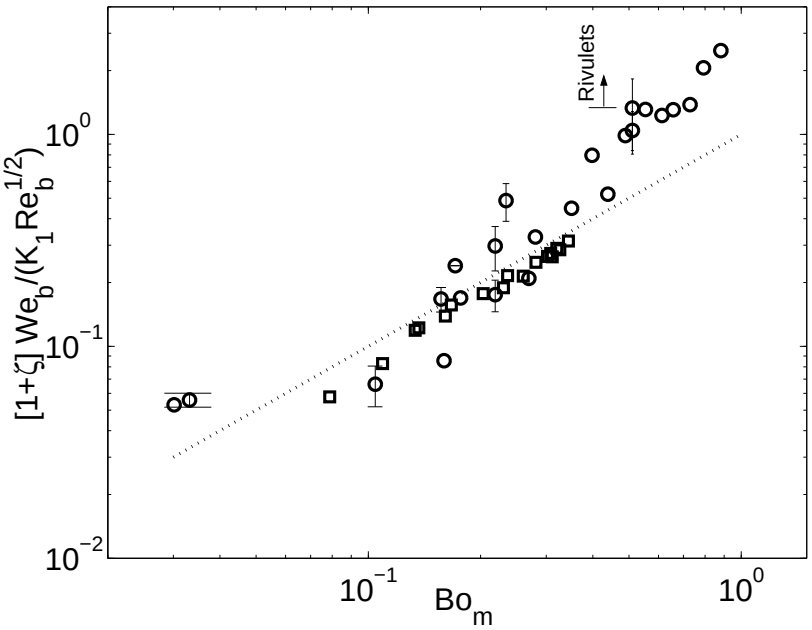

FIGURE 5. Dimensionless velocity as a function of the modified Bond number $Bo_m = Bo_\alpha - Bo_c$, where $Bo_\alpha = \rho V^{2/3} g \sin\alpha/\sigma$ and $Bo_c = c_1 w(\cos\theta_{sr} - \cos\theta_{sa})/V^{1/3}$. ○, water; □, mercury; ..., equation (3.17). $c_1 = 1.5$ and $K_1 = 0.22$ for water while $c_1 = 1$ and $K_1 = 0.18$ for mercury. $c_3 = 1.6$ and $c_5 = 1.8$ for both the fluids.

Equation (3.18) implies that the characteristic velocity scale in the inertial regime is $\left(\sigma^2/\rho R_b \mu\right)^{1/3}$. In the limit when wedge dissipation is dominant, $\zeta \gg 1$, (3.17) reduces to

$$\frac{We_b}{Re_b} = Ca = K_3 Bo_m, \tag{3.19}$$

where $K_3 = 0.0867K/(c_3 \ln(R_b/\lambda) c(\theta_e))$ and $d/2 = KR_b$; (3.19) is the dimensionless form of (3.10), implying that the characteristic velocity scale at low Re is σ/μ. As discussed earlier, (3.18) is valid for $Re \gg 10^3$ for water drops while it holds for $Re \gg 10$ for mercury drops. Equation (3.19) is valid for water when $Re \ll 10^3$, and for mercury when $Re \ll 10$. The crossover in the drop motion from a regime dominated by wedge dissipation to that dominated by boundary layer dissipation occurs at $\zeta \sim 1$. From (3.15), such a condition can be rewritten as

$$\frac{\sqrt{Re_b}}{c(\theta_e)} = 92.5, \tag{3.20}$$

where $c(\theta_e)$ is given by (3.8).

Figure 5 shows that the measured velocities for water and mercury, shown in figure 3, collapse reasonably well when presented in the dimensionless form (3.17). The mercury data are, however, in better agreement with (3.17) than the water data. The deviation of the water data at small velocities is most likely because of the large contact angle hysteresis due to irregularities of the substrate. When the hysteresis is large (35° for the water drops), the critical Bond number ((3.4) and (3.5)) may vary by as much as 10% and this will affect the velocity. In addition, at low velocities, large hysteresis could cause stick and slip phenomena, resulting in larger errors in the measured steady velocities. It is seen in figure 5 that, at large Bo_m, the measured velocities of water drops are larger

than predicted by the force balance model. This would suggest that the contact line force decreases with increasing drop velocity; however, other hydrodynamic explanations might also be possible.

Equations (3.10) and (3.16) for the velocity of the drops, as well as the dimensionless relation (3.17) need to be taken only as scaling laws, valid only in an order of magnitude sense. These equations neglect possible variations of θ_d with velocity, the peripheral variation of the contact line velocity and the variation of θ_d due to this, as well as the effects of change in drop size on the pre-factors and the drop geometry. These equations have undetermined pre-factors, whose values may change from the values suggested in this study when the above effects are considered. Further investigations are necessary to account for these effects on the drop velocity in the inertial regime.

4. Dynamic contact angle

The measured dynamic contact angles for water and mercury as a function of the algebraic capillary number (Ca_A) is shown in figure 6. Ca_A has the same value as Ca but is taken positive for θ_a and negative for θ_r. The variation of θ_d with Ca_A observed by Le Grand *et al.* (2005) is shown as the dashed line in figure 6. There is an asymmetry in the change of θ_r and θ_a; θ_r is a stronger function of Ca_A than θ_a. This asymmetry is more obvious in the inset plot of figure 6 where the variation of the dynamic contact angles is shown after the hysteresis is subtracted. The asymmetry is stronger in mercury than in water. The asymmetry in water is similar to that observed for more wetting viscous drops by Le Grand *et al.* (2005). The flattening out of the curve for mercury at $Ca_A \approx -0.0015$ is due to the corner formation at the rear, to be discussed in § 5.1. In the case of water drops a change in drop geometry occurs at $Ca_A \leqslant -0.0047$ (see later in figures 16 and 15(b)). The error bars in the figure show the range of the dynamic contact angles from repeated measurements. As mentioned earlier, the dynamic contact angles were measured with a resolution of $r_m = 10^{-4}$m. The Reynolds numbers based on r_m and drop velocity are less than 639 for mercury drops and 67.5 for water drops. Even though the local Re decreases as the contact line is approached, the Reynolds numbers based on r_m and drop velocity are appreciable; inertial effects could be important in determining the dynamic contact angles.

4.1. *Comparison of dynamic contact angle models*

To see the effect of these large Re, we now compare our dynamic contact angle variation with the various contact angle models that relate the dynamic contact angles with the dimensionless drop velocity. The dynamic contact angle models considered are,

(*a*) viscous models that have been considered for viscous drops by Le Grand *et al.* (2005),

(*b*) the model by Shikhmurzaev (1993) that is based on the assumption of material flux through the contact line and the associated relaxation of interfacial tension and

(*c*) the inertial model by Cox (1998).

4.1.1. *Justification for comparison with viscous models*

The reasons for comparison of our high Re data with viscous contact line models are the following.

(*a*) Even if the measurement scale is inertial, since the contact angle slowly evolves from the molecular scale - which is certainly viscous - to the measurement scale, the contact angle is determined mostly in a regime that is entirely viscous.

(*b*) As shown in the inset of figure 6, our dynamic contact angle variation with Ca in

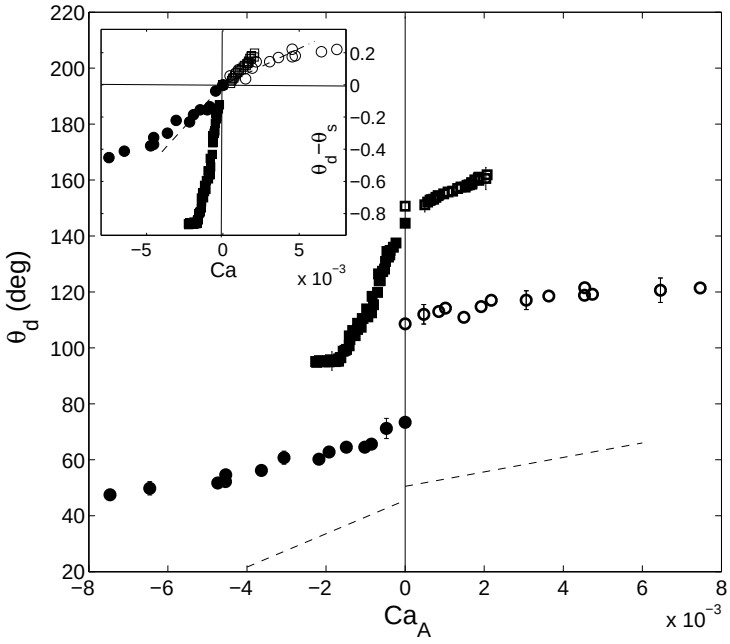

FIGURE 6. Dynamic contact angles as a function of the algebraic capillary number Ca_A; ○,●, advancing and receding contact angles of water drops; □, ■, advancing and receding contact angles of mercury drops. The dashed line is a linear fit through the data of Le Grand *et al.* (2005) at $Re \ll 1$. The inset shows the variation of the dynamic contact angles in radians after the hysteresis is subtracted.

water at high Re practically coincides with that of Le Grand *et al.* (2005) at $Re \ll 1$, implying that there is no Re effect noticed on the contact angles between these two studies at widely different Re. The same can also be noticed from the results of Le Grand *et al.* (2005) where the dynamic contact angles for drop motion at $1.1 \times 10^{-5} < Re < 1.4$ fall on the same curve with respect to Ca in their figure 18.

(*c*) At our measurement resolution $r_m = 100\mu$m, inertia is more than viscous effects since $l_\nu = \nu/U$, the viscous length scale at which $Re_l = Ul_\nu/\nu \sim 1$, is smaller than r_m. Figure 7(a) shows that l_ν is of the order of 2μm to 200μm in water and 0.2 to 2μm for mercury in the corresponding range of Ca. However, the length scale $l_U = (\sigma/\rho)/U^2$, at which the Weber number $We_l = \rho U^2 l_U/\sigma \sim 1$ is larger than the experimental resolution; surface tension forces hence dominate over the inertial effects at our measurement resolution. In addition, the length scale $l_\sigma = \nu^2/(\sigma/\rho)$ corresponding to $Oh^2 \sim 1$, where the Ohnersorge number $Oh = \nu/\sqrt{\sigma/\rho l_\sigma}$, is much smaller than the other length scales. The flow is hence surface tension dominated from large scales till $10^{-2}\mu$m in water and till $10^{-4}\mu$ m in mercury; viscous bending will be low. There will hence be negligible change in the contact angles below the length at which viscous bending becomes important till l_ν. Viscous bending becomes prominent below around 35μm in water and 10μm in mercury at the highest Ca in these fluids, as shown in Appendix A. Even though we are measuring θ_d with a resolution lower than necessary to resolve up to the viscous bending length, it is shown in Appendix A that the change in contact angles due to this is small. Therefore, since inertia is small compared to surface tension effects at r_m and since viscous bending is small, the contact angles measured at r_m could approximately

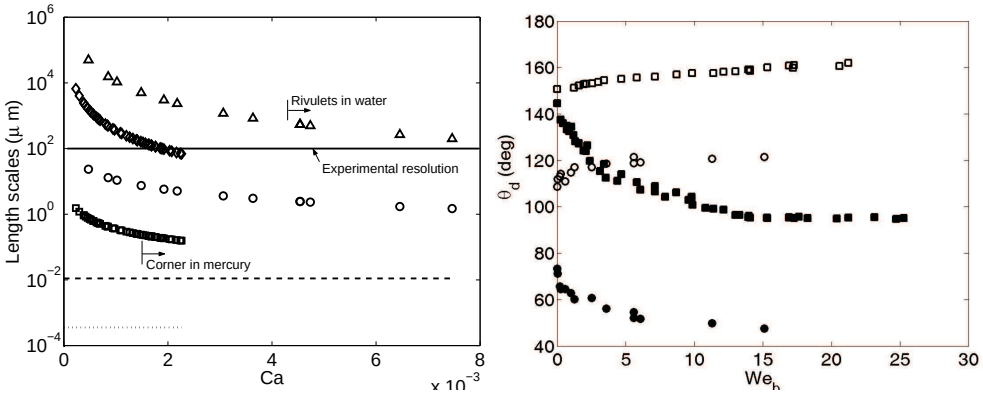

FIGURE 7. a) Variation of different length scales with capillary number. ○, □, length $l_\nu = \nu/U$ at which $Re \sim 1$ for water and mercury; △,◇, length scale $l_U = (\sigma/\rho)/U^2$ at which $We \sim 1$ for water and mercury; −−, ..., length scale $l_\sigma = \nu^2/(\sigma/\rho)$ at which $Oh^2 \sim 1$ for water and mercury. b) Variation of contact angles with the Weber number based on the base radius. ○,●, advancing and receding contact angles in water; □, ■, advancing and receding contact angles in mercury.

be same as that measured at a location l_ν where $Re_l \sim 1$. In other words, even though the Re based on the drop diameter is large in our experiments, the actual Re for contact angles, based on the velocity of the contact line and a local length scale will be small.

(*d*) The measured contact angle variations correlate better (more nearly linear) with Ca rather than We_b, as could be seen by comparing figure 7(b) with figure 6.

4.1.2. *Criteria for the comparison of contact angle models*

The consistency of the examined models with our contact angle data is assessed after all the models are rewritten in the form $f(\theta_s, \theta_d) \sim Ca$. We do not assess the models based on how good the experimental data fits the theory since it is well known that most models fit the dynamic contact angle data if one chooses the parameters in the models to achieve such a fit. Earlier attempts based on the quality of fit of the models with experiments have proved inconclusive (Seveno, Vaillant, Adao, Conti & DeConinck 2009). In addition, such an assessment based on the goodness of fit tells nothing about whether the model and its parameters are physically consistent. Due to these reasons, we follow the following procedure to assess the consistency of various models with our experimental data.

(*a*) The slopes of the plots of $f(\theta_s, \theta_d)$ vs Ca obtained when the various theories are matched to the present data for water and mercury are examined to see whether these are of the same order as suggested by the theories.

(*b*) It is examined whether the models preserve the continuity of slopes at $Ca = 0$ in a plot of $f(\theta_d, \theta_d)$ vs Ca. This is necessary since most of these models do not distinguish between θ_a and θ_r and hence the variation of these angles as $Ca \to 0$ should be the same.

(*c*) It is examined whether the plot of $f(\theta_s, \theta_d)$ vs Ca is the same for water and mercury. If this is not the case, then it is examined whether such a difference is suggested by the theory.

4.2. *The linear model*

The simplest, linear and empirical model is the one proposed by Dussan (1979) which is obtained when f is a first order polynomial in the form,

$$\theta_d - \theta_s \propto Ca_A \tag{4.1}$$

A linear fit matches $\theta_a - \theta_{sa}$ vs Ca_A for $0 \leqslant Ca_A \leqslant 0.0022$ for water with a slope of 58.53. Similarly, a linear fit matches $\theta_r - \theta_{sr}$ for $0 \leqslant Ca_A \leqslant 0.002$ with a slope of 108.23. The corresponding slopes obtained by Le Grand *et al.* (2005) for low contact angle, high viscous silicon oil drop motion are 45.1 and 104.1, very close to the values obtained for water in the present study. As seen in the inset of figure 6, the variation of θ_d with Ca in silicone oil and water drops are the same even though they are at very different Re. The mercury drops show a similar behaviour but with a larger slope of 100 for $0 \leqslant Ca \leqslant 0.002$ in the advancing side and 533 for $0 \leqslant Ca \leqslant 0.0015$ in the receding side. The linearity is observed till corner formation in mercury while the data deviates from a linear curve much before the shape change in water. Hence a linear model (4.1) would approximate the experimental results of figure 6 in a narrow Ca range, but with a different pre-factor for mercury and water and for θ_a and θ_r.

Even though a linear model approximates the dynamic contact angle variation in a short range of Ca, the variation over a larger range of Ca is nonlinear, especially for the water data in figure 6. The non linearity of contact angle variation with Ca is often obvious only in studies that have a range of contact angles spanning both the sides of $\theta_d = 90°$. The drops of Le Grand *et al.* (2005) have a contact angle range of $25° < \theta_d < 65°$ while the present mercury drops have $95° < \theta_d < 162°$; these data appear quite linear in Le Grand *et al.* (2005) and in the present figure 6. The range of water data in the present study is $47.5° < \theta_d < 121.4°$, the nonlinearity is more pronounced for water in figure 6 since θ_d varies over a range around 90°.

Since cosine of the contact angles appear in the force balance in the direction of motion at the contact line, this nonlinear behaviour could be expected to be better approximated by a cosine law. The general cosine model would be of the form,

$$(\cos\,\theta_s - \cos\,\theta_d) f(\theta_d, \theta_s) = K Ca_A, \tag{4.2}$$

where K is a constant. Various contact angle models, derived from widely different assumptions, express their final relation between θ_d and Ca as particular forms of (4.2). Some of these models are Molecular-Kinetic theory (Blake & Haynes 1969), de Gennes model(de Gennes 1986) and Shikhmurzaev's model(Shikhmurzaev 1993); we now look at these models, along with the Cox-Voinov model, in the following sections.

4.3. *Molecular-Kinetic model (Blake & Haynes 1969)*

The simplest cosine law of the form (4.2) is

$$\cos\,\theta_s - \cos\,\theta_d = A_1 Ca_A. \tag{4.3}$$

Equation (4.3) is the molecular-kinetic model for $kT >> (\cos\theta_s - \cos\theta_d)\sigma/n$, where k is the Boltzmann constant, T is the temperature, n is the number of adsorption sites per unit area and A_1 is composed of molecular terms and μ. This model, proposed by Blake & Haynes (1969), assumes that the variations in θ_d are due to changes in adsorption equilibrium at the contact line. The truncated form of this model for small θ_d results in its more popular, second order form,

$$\theta_d^2 - \theta_s^2 = 2A_1 Ca_A, \tag{4.4}$$

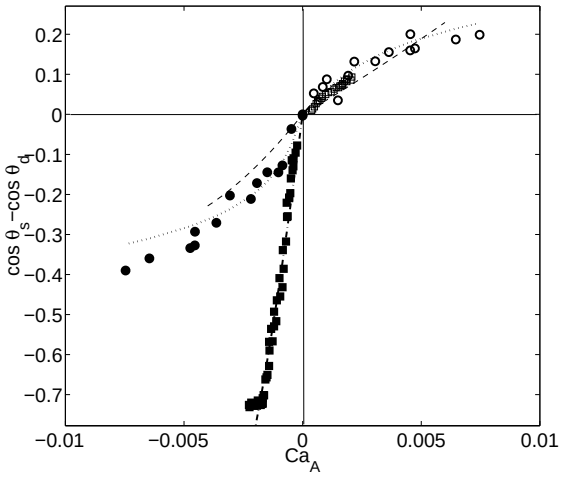

FIGURE 8. Comparison of dynamic contact angles with the molecular-kinetic theory (4.5). ○,●, advancing and receding angles in water; □ ,■ advancing and receding angles in mercury. The dashed line corresponds to the data of Le Grand *et al.* (2005). The dotted lines shows the prediction of molecular-kinetic theory for water with $\Lambda = 0.76$nm, with $\kappa = 8\times10^7\text{s}^{-1}$ for advancing angles and $\kappa = 3 \times 10^7\text{s}^{-1}$ for receding angles. The dashed-dotted line corresponds to the prediction of (4.5) for mercury, with $\Lambda = 0.4$nm and $\kappa = 3 \times 10^8\text{s}^{-1}$ for advancing angles, and with $\Lambda = 0.1$nm and $\kappa = 3 \times 10^9\text{s}^{-1}$ for receding angles.

However, since our experiments are not for large kT, or for small θ_d, we use the general form of (4.3),

$$\cos\theta_s - \cos\theta_d = \frac{kT}{\sigma\Lambda^2}\sinh^{-1}\left(\frac{Ca\sigma}{2\kappa\Lambda\mu}\right), \tag{4.5}$$

valid for all kT and θ_d, given by Blake & Haynes (1969). Here, the two parameters that have to be chosen for the theory to fit the data are Λ the average distance between the centres of adsorption sites and κ the frequency of molecular displacement per unit length of the triple line. Figure 8 shows the comparison of the dynamic contact angle variation suggested by (4.5) with our experimental data. The results of Le Grand *et al.* (2005) are also shown in figure 8. Λ and κ were estimated by trial and error to match the theory with the experimental data, keeping in mind that Λ has to be of the order of the dimensions of the functional groups at the solid surface. Figure 8 shows that, for advancing angles in water, the theory matches the experiment for $\Lambda = 0.76$nm and $\kappa = 8 \times 10^7\text{s}^{-1}$; for receding angles in water the theory matches for the same Λ but with $\kappa = 3 \times 10^7\text{s}^{-1}$. The values of these coefficients are comparable with the values of $\Lambda = 2.4$nm and $\kappa = 4.2 \times 10^6\text{s}^{-1}$ obtained by Bayer & Megaridis (2006) for water on glass under good wetting conditions ($\theta_s = 20°$).

Since Λ is a property of the surface, a common value for the advancing and the receding side is expected. The value of Λ is expected to be of the order of the dimensions of the functional groups on the surface. Glass (SiO_2) has a Si-O bond length of the order of 0.16 nm - 0.18nm (Holleman & Wiberg 2001), implying an approximate molecular size of about 2 times this bond length since the angle between Si and O varies from 140° to 180°. The presence of the long chained FAS mono-layer on the glass surface, which increases the distance between the functional groups, could be the reason for $\Lambda = 0.76$nm that is larger than the molecular size of about 0.4nm. However the need for a different frequency

of molecular displacement for the advancing and the receding motion of the contact line could be contrary to the assumptions behind the model. Note that the surfaces at the advancing and the receding sides of the drops in our experiments are exactly the same because the drops follow the pre-wetted trail left by the earlier drop on the surface. Hence we presume that this need for different κ for the advancing and the receding sides could be because the model neglects any hydrodynamic influence that could cause a difference between the advancing and receding contact lines.

Best fits for mercury on glass were obtained with $\Lambda = 0.4$ nm and $\kappa = 3 \times 10^8 \mathrm{s}^{-1}$ for advancing angles, while $\Lambda = 0.1$ nm and $\kappa = 3 \times 10^9 \mathrm{s}^{-1}$ for receding angles. Even though the magnitudes of Λ are of the same order as the molecular size in glass, the need for different Λ for the advancing and receding sides may be unphysical since Λ is a property of the solid surface. Here too the need for a different value of κ for the advancing and receding sides could be due to the neglect of the hydrodynamic effects in the model. However, recently it has been pointed out that the Molecular-Kinetic model could hold at the scale of surface defects(Rolley & Guthmann 2007). In such a case the values of κ and Λ could be quite different from those expected by the original model. It might also be possible that differences in wetting at the advancing and receding surfaces could change the value of the surface property Λ; however these issues have to be investigated further.

The molecular-kinetic theory groups the advancing contact angle data for Si oil, water and mercury, implying that all these fluids have approximately similar values of Λ and κ. However the receding parts of the curve in figure 8 show different behaviours for the different fluids, the values of Λ and κ for these fluids are widely different from each other. Further, asymmetry and discontinuity of slope at $Ca = 0$, strong for the case of mercury, remains for the data, implying that the same fluid will need different values of these parameters for the advancing and receding arms.

Note that the advancing contact angles of Le Grand *et al.* (2005) at $Re \ll 1$ coincide with the present results for water drops and mercury at $Re \sim 10^3 - 10^4$; the variation is also linear in Ca to first order. This indicates that the contact line dynamics does not depend on Re. The receding contact lines of all the three fluids have different behaviours with Ca from each other. However, it is unlikely that this is a Reynolds number effect because the variation of advancing contact angles coincides with that of low Re drops. As will be seen in § 4.6, one possible explanation is the difference in the surface velocity between the receding and the advancing sides between the three fluids, a hydrodynamic effect not considered by the molecular-kinetic model. Such a difference is possibly not an inertial effect, but a consequence of the difference in geometry of the drops between the advancing and the receding sides, the effect being amplified in mercury drops due to their larger contact angles.

4.4. *de Gennes model (de Gennes 1986)*

The non-truncated de Gennes model, which uses the Poiseuille flow approximation for the flow near the contact line and is valid for larger contact angles, is of the form,

$$\theta_d(\cos\,\theta_s - \cos\,\theta_d) = 3\ln(R_b/\lambda)Ca_A. \tag{4.6}$$

Comparison of (4.2) and (4.6) makes it clear that $f(\theta_d) = \theta_d$ and $K = \pm 3\ln(R_b/\lambda)$ for this model. Using the small angle approximation $\cos\theta = 1 - \theta^2/2$ for the cosines in (4.6) gives,

$$\theta_d\left(\theta_d^2 - \theta_s^2\right) = 6\ln\left(R_b/\lambda\right)Ca_A, \tag{4.7}$$

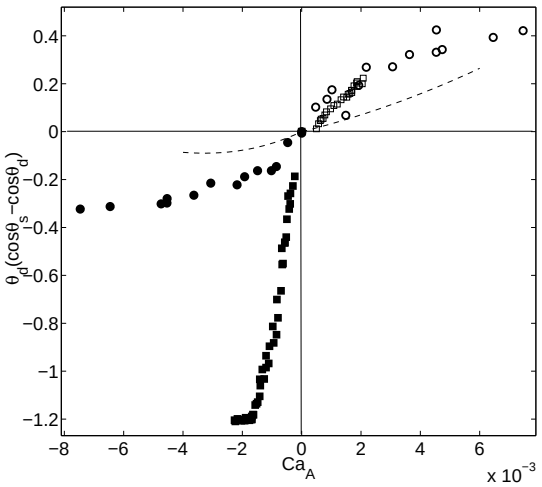

FIGURE 9. Comparison of the measured contact angle variations with the de Gennes model (4.6); ○,●, advancing and receding angles in water; □ ,■ advancing and receding angles in mercury. The dashed line corresponds to the data of Le Grand *et al.* (2005).

the more popular form of the third order model, valid for small contact angles. The model was proposed based on a local force balance at the triple line using a Poiseuille flow assumption. Figure 9 shows that the water data agree with (4.6) only with the pre-factor 10^2, instead of the expected slope of $3\ln(R_b/\lambda) = 39$, shown by the data of the viscous drops of Le Grand *et al.* (2005) in the figure. The corresponding slip length is 1×10^{-17} m, an unphysically small length; the slip lengths in mercury will be even smaller. The asymmetry and the discontinuity of slope at $Ca = 0$ of the water data is now removed, but these persist for mercury. The multiplication by θ_d in (4.6) simply implies that the velocity gradient is approximated by $U/r\theta_d$, where r is measured from the contact line (de Gennes, Brochard-Wyart & Quere 2004). In other words, the model is derived from the assumption that the height of the interface at any distance x from the contact line $h(x) = \theta_d x$, implying that viscous bending is neglected (Eggers 2004). The reason for the discrepancy of the model could be that when $\theta_d > 90°$, which is the case for the mercury drops, and partly for the water drops, this approximation is no longer valid.

4.5. *Cox-Voinov Model (Cox 1986, 1998; Voinov 1976)*

We now compare the dynamic contact angle data with the viscous, third order model,

$$\theta_d^3 - \theta_s^3 = 9\ln(R_b/\lambda)Ca, \tag{4.8}$$

called the Cox-Voinov law, proposed by Voinov (1976) and Cox (1986), which is valid for $\theta_d < 3\pi/4$. The above model is based on a model for slip at the contact line, along with viscous bending of the liquid-gas interface that changes the microscopic contact angle θ_m to the measured apparent contact angle θ_d; θ_m is often assumed as equal to θ_s. The comparison of (4.8) with the present dynamic contact angle data is shown in figure 10(a). The slope of the linear fit for water, valid only for $-0.0025 < Ca_A < 0.005$ is 560, implying that the slip length is 2.9×10^{-30}m, an unphysical, sub-atomic length. Note that the maximum θ_d for water in the experiments is 121° so that the model is valid for the whole range of our data, if the local Re is less than one. For mercury, the

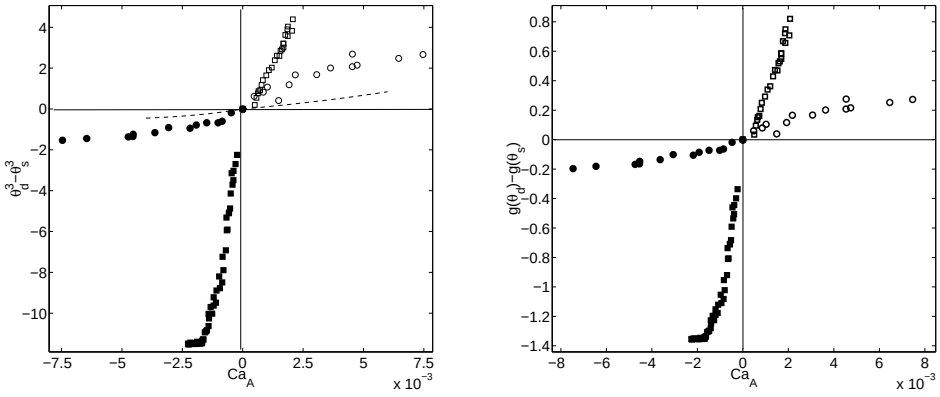

(a) (b)

FIGURE 10. Comparison of dynamic contact angle variation with the Cox-Voinov model (a) Comparison with (4.8), valid for small θ_d. Dashed lines are the fit suggested by Le Grand *et al.* (2005). (b) Comparison with (4.9), valid for arbitrary θ_d. ○,●, advancing and receding angles in water; □ ,■ advancing and receding angles in mercury.

model is valid only for the receding contact angles since the advancing angles, $\theta_a > 3\pi/4$. For receding angles in mercury, figure 10(a) shows that the slope of a linear fit is around 4000, implying that the slip length is about 1.7×10^{-196}m, a length scale smaller than even the size of the smallest elementary particle. The slip length found out by Le Grand *et al.* (2005) for the data for 10cP Silicone oil, shown in the figure as dashed line, was 3 nm. The decrease in slip length with ν for Si oils, noticed by Le Grand *et al.* (2005), seems to continue to unphysically small values with further lower values of ν as in the case of water and mercury.

At the high Re values of the present drop motion experiments, viscous losses occur mainly at length scales of the order of the boundary layer thickness δ. Hence, δ, instead of R_b, might be the appropriate length scale to be used in (4.8). Estimating the slip length λ that would be required when using $\ln(\delta/\lambda)$ instead of $\ln(R_b/\lambda)$ in (4.8) gives $\lambda = 6.3 \times 10^{-32}$ to 2.5×10^{-31} m for water and $\lambda = 1.5 \times 10^{-198}$ to 4.95×10^{-198} m for mercury. These are even smaller values of λ than required when R_b is used as the macroscopic length scale.

Equation (4.8), valid only for $\theta_d < 3\pi/4$, is a simplified form of the general relation,

$$g(\theta_d) - g(\theta_s) = Ca \ln(R_b/\lambda), \tag{4.9}$$

proposed by Cox (1986) for arbitrary contact angles, where

$$g(\theta) = \int_0^\theta \frac{x - \sin x \cos x}{2 \sin x}\, dx. \tag{4.10}$$

Figure 10(b) shows our data for water and mercury plotted in terms of $g(\theta_d) - g(\theta_s)$ vs Ca_A, the slope of the curves giving the value of $\ln(R_b/\lambda)$. The slope of the curve for water is 50, implying that the slip length $\lambda = 5.8 \times 10^{-25}$m. Similarly the slope of the curve of mercury is about 600 implying that $\lambda = 4.64 \times 10^{-264}$m; the obtained slip lengths are unphysically small, as in the case of the truncated model (4.8).

The Cox-Voinov law makes the slope of the advancing and the receding part in figure 10(a) same at $Ca = 0$ for both water and mercury. However, to fit the theory to our data with $\theta_m = \theta_s$, one would need slip lengths that are quite unphysical for water and

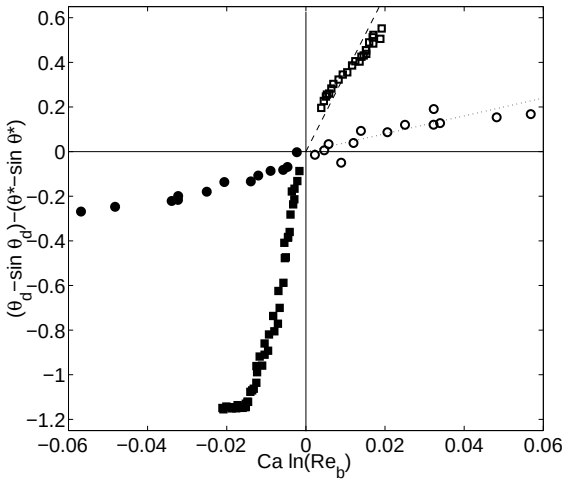

FIGURE 11. Variation of dynamic contact angles according to Cox inertial model (4.11); ○, ●, advancing and receding angles in water; □, ■, advancing and receding angles in mercury. The dotted line is of slope 4, while the dashed line is of slope 35.

mercury; these lengths will also need to be quite different for both fluids. If θ_m is also to be adjusted so as to make the slip lengths approximately same for water and mercury and of the expected order of magnitude, one would need an additional model, namely the molecular-kinetic model discussed in § 4.3, to include the variation of θ_m, as has been done by Petrov & Sedev (1992). However, even this approach has been shown to need unreasonably small λ and large Λ to match the experimental results in various alcohols (Petrov, Ralston, Schneemilch & Hayes 2003). Now again, if the Molecular-Kinetic model holds at the level of surface defects, as suggested by Rolley & Guthmann (2007), it may be possible to justify the unreasonable values of the parameters of the model. Similar difficulties with the Cox-Voinov theory when applied to water drops have recently been reported by Winkels *et al.* (2011).

The above two models by Voinov (1976) and Cox (1986) are for viscous flows near the contact line when the local $Re < 1$. We tested these models for our high Re drop motion, like other previous viscous models, due to the reasons discussed earlier in § 4.1.1. We now compare our results with the only contact angle model that explicitly includes Re effects, namely the inertial model of Cox (1998). The model is valid only for advancing contact angles. The case of interest is $1 \ll Re \ll \varepsilon^{-1}$, where $\varepsilon = s/R_b$ with $s \equiv \lambda$. For these conditions and $Ca\ln(1/\varepsilon Re) \ll 1$, the Cox model leads to the expression.

$$(\theta_d - \sin\theta_d) - (\theta^* - \sin\theta^*) = \frac{1}{1.5316} Ca_A \ln Re_b \tag{4.11}$$

where, θ^* is given by $Ca\ln(1/\varepsilon Re_b) = g(\theta^*) - g(\theta_s)$ and $g(\theta)$ is given by (4.10). The comparison of (4.11) with experiments is shown in figure 11. The advancing contact angles of water can be fitted with a pre-factor for $Ca\ln Re_b$ equal to 4, which is an order of magnitude higher than the expected pre-factor from the theory of $1/1.5316 = 0.653$. Further, the mercury data do not coincide with water and would need a pre-factor of 35 for the advancing part instead of 0.653. The inertial model by Cox (1998) seems to be predicting a much lower variation of θ_d with velocity than observed in the present experiments.

4.6. *Model by Shikhmurzaev (1993)*

The model proposed by Shikhmurzaev (1993) is a set of boundary conditions obtained by considering a material flux across the contact line thereby avoiding the singularity at the contact line. This material flux makes a fluid element in the liquid-gas interface to become part of the solid-liquid interface over a surface tension relaxation time τ, resulting in a change in the interfacial tension from its equilibrium value. Using these boundary conditions, analytical solutions for Stokes equations have been found by Shikhmurzaev (2008) when $Ca \to 0$. This solution is valid at such distances from the contact line at which the Re based on this length is small, while the distance itself is much larger than the surface tension relaxation length $U\tau$. For negligible surface tension between the solid and the gas, the solution given by Shikhmurzaev (2008) is,

$$(\cos\,\theta_s - \cos\,\theta_d) f(\theta_d)/Sc = Ca, \tag{4.12}$$

where

$$f(\theta_d) = \sqrt{\frac{1 + (1-\rho_G^s)\cos\,\theta_s}{4(\cos\,\theta_s + B)(\cos\,\theta_d + B)}}, \tag{4.13}$$

$$B = \frac{1 + \rho_G^s u_{12}(\theta_d)}{1 - \rho_G^s}, \tag{4.14}$$

$$u_{12}(\theta_d) = \frac{\sin\,\theta_d - \theta_d \cos\,\theta_d}{\sin\,\theta_d \cos\,\theta_d - \theta_d} \tag{4.15}$$

is the free surface velocity, normalised by the drop velocity, obtained from the corner flow solution of the Stokes equations and $\rho_G^s = \rho_e^s/\rho_0^s$ is the ratio of equilibrium surface density to the surface density corresponding to zero surface tension. The coefficient Sc in (4.12) depends on the physical properties as follows

$$Sc = \sqrt{\frac{\sigma^2 \tau \beta}{\mu^2 \gamma \rho_0^s (1 + 4\alpha\beta)}} = \sqrt{\frac{\sigma\tau(1-\rho_G^s)}{5\mu\epsilon}}. \tag{4.16}$$

Here, α is the phenomenological coefficient that describes the effect of surface tension gradient on the velocity distribution in the interfacial layer near the solid, β is the coefficient of sliding friction (Lamb 1932) so that $\alpha\beta = 1$ and ϵ the interfacial layer thickness. $\gamma = \sigma(1-\rho_G^s)/\rho\epsilon$ is the phenomenological coefficient in the surface equation of state

$$\sigma(\rho^s) = \gamma(\rho_0^s - \rho^s), \tag{4.17}$$

that reflect the assumption of the model that the compression of the surface phase, resulting in a change in the surface density ρ^s, results in a decrease of surface tension near the contact line. The key difference of Shikhmurzaev's model from the other models in the small Ca limit is that, as per the model, the contact angles are not just functions of the contact line speed, but also of the dimensionless velocity at the liquid-gas interface, seen as u_{12} in the term B in (4.13). The interface velocity comes in the model because the model considers contact line motion as essentially a process by which liquid-gas interface disappears to become a solid liquid interface, the rate at which this occurs is decided by the velocity of the fluid in the liquid-gas interface.

To compare equation (4.12) with experiments, we need the values of ρ_G^s and Sc. The effect of changing ρ_G^s is to stretch the data distribution along the ordinate, while a change in Sc rotates the data around the origin. Multiple combinations of ρ_G^s and Sc would make a plot of the left hand side of equation (4.12) vs Ca with slope one, and only ranges of these parameters are known a priori. Due to such a difficulty in knowing the values of the

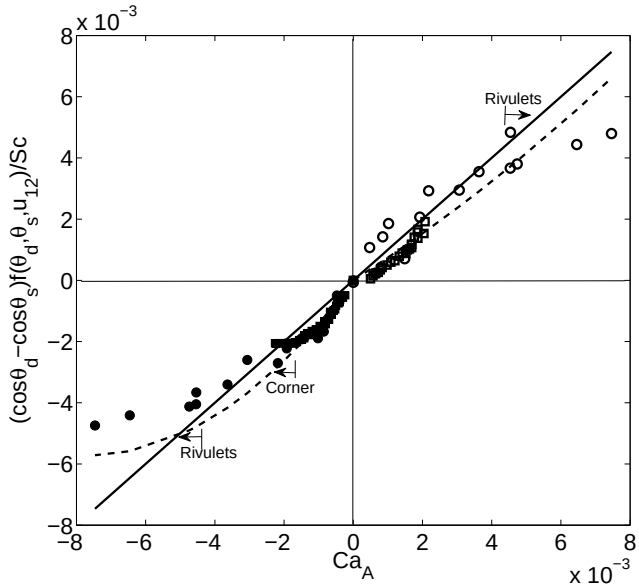

FIGURE 12. Comparison of the dynamic contact angle variation with the model of Shikhmurzaev (1993)(4.12) using $\rho_G^s = 0.98$ and $Sc = 1, 1.7$ and 10 for Si oil, water and mercury respectively. ○, ●, advancing and receding angles in water; □, ■, advancing and receding angles in mercury. The dashed line is the data of Le Grand *et al.* (2005). The solid line is of slope one corresponding to (4.12).

parameters of the model a priori to a fit with the experimental data, Shikhmurzaev (2008) suggests to take Sc as an adjustable parameter once a value of ρ_G^s is fixed. Following a similar route, we first estimate the value of $\rho_G^s = 0.98$ in Appendix C and then chose the values of Sc that make the experimental data of each fluid, plotted in terms of left hand side of (4.12) vs Ca, an approximately linear curve of slope one. It is then verified that the values of τ given by these values of Sc are of the order suggested by the theory.

Figure 12 shows the comparison of equation (4.12) with our experimental data, as well as with the data of Le Grand *et al.* (2005), using $\rho_G^s = 0.98$ and $Sc = 1, 1.7$ and 10 respectively for Si oil, water and mercury. Before the onset of corner or rivulets, the data group reasonable well around the solid line of slope one. τ can now be estimated from these values of Sc and ρ_G^s using (4.16). We find that $\tau = 27$ns, 0.24μs and 0.45μs for water, mercury and Si oil. The relative magnitude of these values match the estimate of $\tau \propto \mu$, suggested by Shikhmurzaev (2008), showing the diffusive nature of surface tension relaxation. These values are also within the continuum limit and similar to the estimates of Shikhmurzaev (2008) for similar viscosities. As per (4.16), $Sc \propto \sqrt{\sigma}$, therefore Sc_{Hg}/Sc_{sioil} should approximately be equal to $\sqrt{\sigma_{Hg}/\sigma_{sioil}}$. However, $\sqrt{\sigma_{Hg}/\sigma_{sioil}} \approx 5$ while, with the values of Sc obtained, $Sc_{Hg}/Sc_{sioil} = 10$. This discrepancy occurs because we have used the same value of $\rho_G^s = 0.98$ for all the fluids for convenience, eventhough the upper estimates of ρ_G^s for the three fluids are different, as shown in Appendix C. Since Sc is a function of ρ_G^s by (4.16), these inexact values of ρ_G^s will result in inexact values of Sc too. The theoretical upper estimate of ρ_G^s for mercury is 0.99. If we use $\rho_G^s = 0.99$ and adjust Sc to fit the theory to the contact angle data of mercury, we obtain a similar fit as in figure 12 with $Sc = 5$. Now, $Sc_{Hg}/Sc_w \approx \sqrt{\sigma_{Hg}/\sigma_w}$ and $Sc_{Hg}/Sc_{sioil} \approx \sqrt{\sigma_{Hg}/\sigma_{sioil}}$.

Hence, we conclude that the values of the adjustable parameters ρ_G^s and Sc that

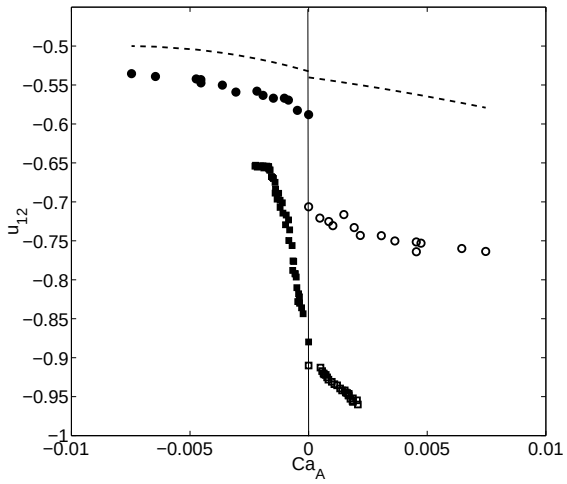

FIGURE 13. Variation of the dimensionless free surface velocity (4.15) with Ca. ○, ●, advancing and receding angles in water; □, ■, advancing and receding angles in mercury. The dashed line is u_{12} for the data of Le Grand *et al.* (2005).

achieve grouping of the data in figure 12 are consistent with the estimates suggested by the theory, even though only order of magnitude estimates of τ and ϵ, and not their exact values, could be obtained. Considering the widely different fluid properties, the grouping of the data shown in Figure 12, while preserving the continuity of slope of one at $Ca = 0$, achieved by the model by using reasonable values of its parameters ρ_G^s and Sc is remarkable. However, it needs to be mentioned here that the theory itself is apparently controversial as could be gauged from the criticisms raised by (Eggers & Evans 2004; Pismen 2011; Henderson 2011; Thiele 2011) and the responses by Shikhmurzaev & Blake (2004) and Shikhmurzaev (2011*a*,*b*,*c*).

Since the main difference of this model from the other models is the dependence of the contact angles on the interfacial velocity, we now examine whether the variation of the interfacial velocity with Ca in these three experiments could account for the ability of the model to group the data. Figure 13 shows the variation of the dimensionless interfacial velocity at the liquid-air interface with Ca, evaluated from (4.15) for the three fluids. As mentioned earlier, the dynamic contact angles corrected for the hysteresis ($\theta_d - \theta_s$) of Le Grand *et al.* (2005) coincided with those observed for water in our experiments at the same Ca, even though the Re are widely different. However for mercury, $\theta_d - \theta_s$ was different at the same Ca at widely different Re from water; a cosine representation as in (4.5) or (4.6) collapsed the advancing angles, but not the receding angles. Comparison of figure 13 with figure 6 shows that the dimensionless free surface velocity of silicon oil, water and mercury show a similar behaviour as that of the dynamic contact angles in these fluids. Not just the relative magnitudes of the free surface velocities at any Ca, but also their variation with Ca is similar to the corresponding dynamic contact angle variation. Consideration of this feature and its effect on the dynamic contact angle variation seems to be the reason why the model by Shikhmurzaev (1993) is able to group the dynamic contact angle variation of viscous silicon oil drops, water and mercury onto a same curve as shown in figure 12.

5. Shape of the drops and wetting transition

5.1. *Shape of the mercury drops*

The side and top views of mercury drops for different Ca are shown in figure 14. Based on the shape changes of the receding contact lines seen in the top views, the following three distinct regimes can be identified,

(a) oval or rounded contact line shape (figure 14a),
(b) corner regime (figure 14b) and
(c) cusp regime (figure 14c).

At larger velocities, the cusp gives rise to a rivulet.

The Ca of oval to corner transition can be determined from the curvatures of the contact line as seen in the top views. These curvatures at the advancing (κ_a) and the receding (κ_r) sides of the drops are defined as the inverse of the radius of the contact line in the top views. Figure 15(a) shows the variation of κ_a/κ_o and κ_r/κ_o with Ca, where κ_o is the curvature at $Ca = 0$. $\kappa_o = 200$ m^{-1} for water drops and $\kappa_o = 450$m^{-1} for mercury drops. At $Ca = 0.0015$, a sharp change in κ_r occurs for mercury drops which coincides with the corner formation in the top view images of figure 14(b). The corner in the present case does not look in the side views like a cone extending all the way to distances of order R_b with its apex at the receding contact line, as in the case of high viscosity, low surface tension fluids of Le Grand *et al.* (2005). The receding contact angle observed in the side views after corner formation is finite and greater than 90°, as seen in figures 14(b) and 14(c). The free surface profile of the receding part in the side view does not have a constant slope and resembles a cone with a rounded tip as shown in the figure 14(b). Cusp formation starts at a capillary number of 0.0021 and a rivulet emerges at 0.0022.

5.2. *Shape of the water drops*

The evolution of the shapes of the water drops on FAS coated glass at different Ca is shown in figure 16. The corresponding curvature changes of the advancing and the receding contact lines in the top view are shown in figure 15(a). As Ca increases, the curvature at the rear in the top view of the drop increases slowly until a rivulet appears at the back when $Ca \geqslant 0.0043$. Unlike in the case of Hg-glass in the present study, as well as in the case of silicon oil drops on glass investigated by Le Grand *et al.* (2005), no sharp shape change of the contact line at the rear to a corner is observed. As can be seen in figure 16, the rear contact line is practically rounded until a rivulet forms in figure 16(f). With increasing Ca, the length of the rivulet at the back of the contact line increases. The surface tension of water is 7 times smaller than that of mercury; we would expect an easier formation of sharp changes in curvature in water than in mercury. However, as we show later in § 5.3, the corner formation seems to be decided more by the inability of the rear contact line to move beyond a maximum speed. The heterogeneity of the solid surface in the case of water drops tends to pin the receding contact line, thereby dragging the receding contact line beyond this maximum speed and preventing a corner from being formed.

5.3. *Wetting Transition & Maximum de-wetting speed*

We consider the corner formation at the rear as the wetting transition, similar to that in Le Grand *et al.* (2005). As discussed in § 5.1 and § 5.2, corner formation occurs only in the case of mercury on glass in our experiments. The corner forms at finite receding contact angle $\theta_{rc} = 95°$ (see figure 14(b)); the ratio $\theta_{rc}/\theta_{sr} = 0.657$. Corner formation is often interpreted to be due to a maximum limiting speed at which the contact line

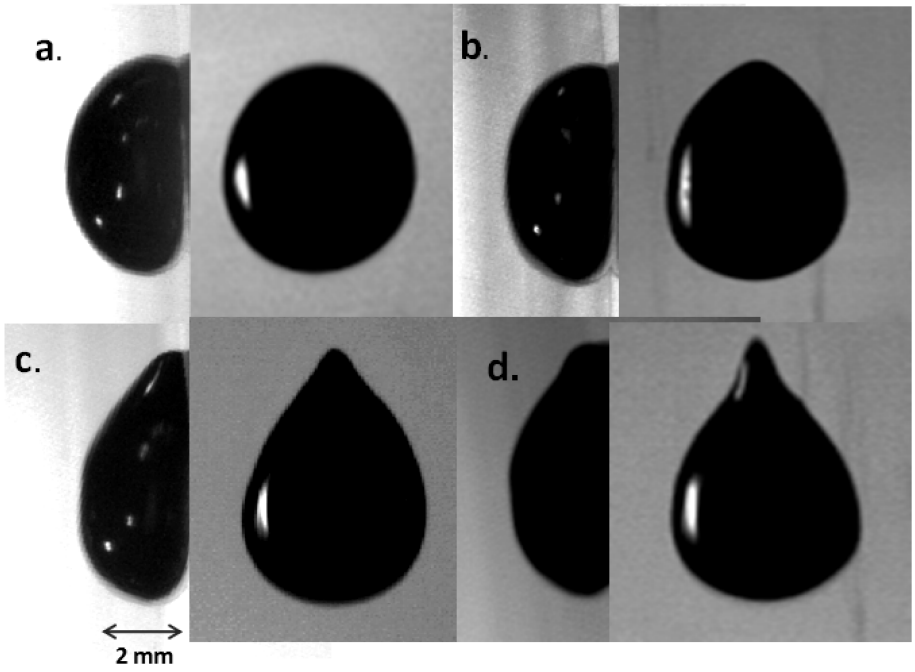

FIGURE 14. Side and top views of the mercury drops at different capillary numbers; (a), oval or rounded at $Ca = 1.1 \times 10^{-3}$, $Re = 9842$; (b), corner formation at $Ca = 1.6 \times 10^{-3}$, $Re = 14553$; (c), cusping at $Ca = 1.9 \times 10^{-3}$, $Re = 16752$ and (d), rivulet formation at $Ca = 2.3 \times 10^{-3}$, $Re = 20069$ respectively.

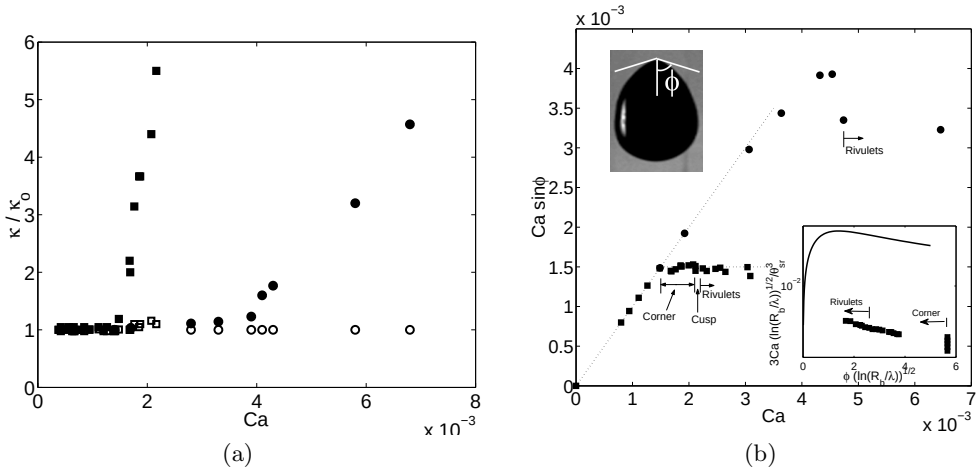

FIGURE 15. (a), Variation of the dimensionless curvatures measured from the top views at the front and rear side as a function of the capillary number; ○, ●, advancing and receding sides of water drops; □, ■, advancing and receding sides of mercury drops. (b), Variation of the dimensionless velocity of the angular contact lines at the rear with the dimensionless velocity of the drop. Inset (i) shows the definition of the corner half angle ϕ while inset (ii) shows the comparison of evolution of ϕ with Ca in mercury with the relation proposed by Snoeijer *et al.* (2007).

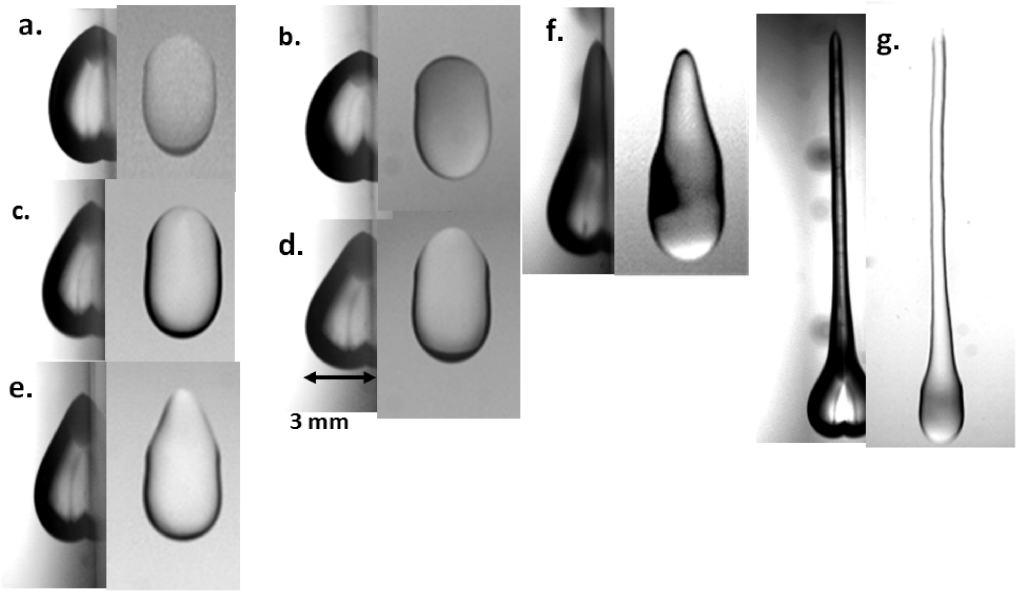

FIGURE 16. Side and top views of the water drops; (a), $Ca = 0.0015$, $Re = 626$; (b), $Ca = 0.0019$, $Re = 809$; (c), $Ca = 0.0036$, $Re = 1531$; (d), $Ca = 0.0043$, $Re = 1819$; (e), $Ca = 0.0045$, $Re = 1910$; (f), $Ca = 0.0047$, $Re = 1995$ and (g), $Ca = 0.0065$, $Re = 2719$.

can recede. If ϕ is the half angle at the rear of the drop in the top view (see the inset of figure 15(b)) the velocity of the receding contact line is $U \sin\phi$. Figure 15(b) shows the dimensionless receding contact line velocity $Ca \sin\phi$ as a function of the dimensionless drop velocity Ca. For mercury drops, till a corner forms at the rear at $Ca = 0.0015$, the receding contact line moves at the same speed as the drop; $Ca \sin\phi = Ca$ in figure 15(b). For $Ca > 0.0015$, $Ca \sin\phi = 0.0015$, the receding contact line moves with a constant speed normal to itself even when the drop velocity is increased. Once the corner is formed, the rear half angle ϕ decreases as $1/Ca$ so that the speed of the rear contact line normal to itself remains a constant, as was first observed by Blake & Ruschak (1979).

If the contact angle is only a function of the contact line speed, as is often assumed in various dynamic contact angle models, then the contact angle that the angular contact lines at the rear makes should remain constant after corner formation. Since the corner forms at $\theta_r = 95°$, $\theta_{sr} - \theta_r = 0.8652$ rads after the corner has formed for mercury drops. Hence the observation that the dimensionless velocity of the contact line $Ca \sin\phi$ is a constant equal to 0.0015 from figure 15(b) gives us an expression for the variation of the corner half angle ϕ after the corner has formed as

$$\sin\phi \approx \frac{\theta_{sr} - \theta_r}{576.8\, Ca}. \tag{5.1}$$

Equation (5.1) uses the assumption that the contact angles are linear functions of the Ca, as in the empirical linear model by Dussan (1979); similar relations could be obtained by using other contact angle models as in Le Grand *et al.* (2005). A comparison of the evolution of ϕ with Ca in our mercury drops with that proposed by (Snoeijer *et al.* 2007) is shown in the inset of figure 15(b). The evolution is qualitatively similar, but quantitatively different by two orders of magnitude. This discrepancy is not surprising since the model by Snoeijer *et al.* (2007) uses Cox-Voinov law, which does not match with the contact angle data in our mercury drops. Further, ϕ at transition to rivulet occurs

close to 45° in mercury drops while the theory by Snoeijer predicts a rivulet transition at $\phi \approx 15°$. This discrepancy too is not surprising since the theory is valid only for small ϕ, whereas ϕ for mercury is close to 90°.

In the case of water drops on FAS coated glass, there appears to be no corner formation at the rear, as was shown in § 5.2. This behaviour is also reflected in the velocity of the angular contact line at the rear of water drops shown in figure 15(b). The velocity of the angular contact line is the same as the velocity of the drop, till it suddenly decreases and remains constant at the formation of a rivulet. It appears that the surface imperfections that cause the hysteresis also drag the contact line, to move it at the drop velocity till rivulet formation. Once a rivulet is formed, further increase in drop velocity increases the length of the rivulet, the rear contact line moving at a constant dimensionless velocity $Ca \sin \phi = 0.003$.

6. Conclusions and Further Discussions

The two primary and important conclusions that emerge from the present experimental study of high Reynolds number (Re), partially non-wetting drops on inclined boundaries at small Capillary numbers (Ca) are:

(a) At high Re the velocity of the drops is governed by the driving gravitational force, the contact line resistance and the predominant boundary layer friction force.

(b) Inertia is negligible in the contact angle variation, which scales with Ca as it does in low Re drop motion; Re effects would be of second order.

These results were obtained with water drops on Fluoro-Alkyl Silane (FAS) coated glass and mercury drops on glass. The range of Ca for water drops is, $0.0003 < Ca < 0.0075$, with inclination angles, $26° < \alpha < 65°$, and the dynamic contact angles $54° \leqslant \theta_d \leqslant 121°$, resulting in a Reynolds number range of $137 < Re < 3142$. For mercury drops on glass, $0.0002 < Ca < 0.0023$, the inclination angles, $5.5° < \alpha < 14.3°$ and the contact angles $92° \leqslant \theta_d \leqslant 160°$, so that $3037 < Re < 20069$.

When $Re \gg 10^3$ for water and $Re \gg 10$ for mercury, or alternatively, when $\zeta = 92.5c(\theta_e)/\sqrt{Re_b} \ll 1$ for both drops, the flow inside the drop is a boundary layer flow as shown in § 3.3. The drop velocity then scales as $Ca\sqrt{Re_b} \sim Bo_m$ (3.18), where Re_b is the Reynolds number based on the base radius and Bo_m (1.2) is the modified Bond number. The general velocity relation $Ca\sqrt{Re_b}(1+\zeta) \sim Bo_m$ (3.17) includes the above asymptote at high Re, as well as the well known low Re asymptote $Ca \sim Bo_m$.

The dependency of dynamic contact angles, corrected for hysteresis, $(\theta_d - \theta_s)$, on Ca of water drops at the present high Re coincides with that observed in silicone oil drops by Le Grand *et al.* (2005) at $Re \ll 1$ in the same Ca range. However, for mercury drops, such a similarity with water in the variation of $\theta_d - \theta_s$ with Ca is observed only for the advancing contact angles; the receding contact angles behaved differently, but its variation is sill linear in Ca. Molecular kinetic theory(Blake & Haynes 1969) is able to capture this variation of contact angles, however with different frequencies of molecular displacement in the advancing and the receding sides for the same fluid-surface combination. For the case of mercury drops, in addition, the average distance between the adsorption sites, a property of the surface, would also have to be different in the advancing and the receding sides. We expect this behaviour of the theory to be due to its neglect of the hydrodynamic factors that could cause a difference between the receding and the advancing sides. We find that the de Gennes' model (de Gennes 1986), the Cox-Voinov model (Voinov 1976; Cox 1986) and the inertial Cox model (Cox 1998) are not able to explain the behaviour of contact angles in water and mercury with pre-factors of the order expected from these theories. The interface formation theory of Shikhmurzaev

(1993) is able to account for the similarity of behaviour between water and silicone oil, as well as the difference in behaviour between water and mercury, by bringing in the free surface velocity and two adjustable parameters ρ_G^s and Sc as parameters that influence the variation of θ_d. The magnitudes and variation of the dimensionless interfacial velocity u_{12} with Ca in the three fluids are similar to the variation of θ_d, which accounts for the different behaviour of θ_d with Ca of these drops.

The mercury drops exhibit a sharp transition from oval shape to a corner at the rear, which happens at a finite receding contact angle of $\theta_{rc} = 95°$. This wetting transition is due to the maximum limiting speed for the moving contact line. The corner to cusp transition happens at a corner angle of 45°. It is of interest to point out that by replacing the viscous dissipation in de Gennes model by an estimate of the corner flow solution of Huh & Scriven (1971), a value $\theta_{rc}/\theta_{sr} = 0.635$ is obtained that is close to the experimentally observed ratio of 0.657. However, as one of the Referees pointed out, the finite contact angle at transition predicted by de Gennes model is a result of mathematical simplification (Eggers 2004) and is, therefore, artificial. Thus, the agreement with experiments, when replacing the viscous dissipation by a corner flow, might just be coincidental. Such sharp shape transitions are not clearly apparent in the case of water drops on FAS coated glass. Due to high pinning of the receding contact line, the receding part tends to directly transform into a rivulet with increasing Ca. Corner formation cannot be excluded entirely in water drops, but if it exists, it occurs over a very narrow range of Ca.

The behaviour of high Reynolds number drop motion observed in our experiments is, in general, consistent with the models developed. Nevertheless, some questions can be raised concerning the contact line resistance in the theoretical expressions (3.16) and (3.17). It is often assumed that the contact line resistance is independent of velocity and is given by the contact angle hysteresis. This assumption is well supported by experiments, usually at low drop velocities. If the contact line resistance were to depend on dynamic contact angles and thereby become a function of velocity, in our experiments, this dynamic contact line resistance alone would nearly compensate the gravitational force and the drop would never move. As figure 5 indicates, the observed drop velocities at large Bo_m are larger than those predicted by the model, which would suggest that the contact line resistance actually decreases with velocity. A possible decrease of interfacial tension at the contact line, as suggested by Shikhmurzaev (1993), would be compatible with a decreasing contact line resistance with velocity. However, hydrodynamic explanations, like the beginning of a global rolling motion as suggested by Mahadevan & Pomeau (1999) is also likely. Further studies with drops of different sizes would be of interest to clarify these questions. In such a case the pre-factors proposed in the present study may become functions of the drop size due to the change in drop geometry with its size. Similarly, if the contact angles are strongly influenced by the free surface velocity, one would expect this influence to be reflected in the variation of contact angles in drops of different sizes.

EJH acknowledges the financial support by IIT Madras while being a Visiting Professor at the Dept. of Applied Mechanics. VSK acknowledges the financial support of Tata Consultancy Services.

Appendix A. Effect of measurement resolution on contact angles

The resolution of our measurements of contact angles (100 μm) is not high. However, we show below that since our experiments are at low $Ca(< 0.0075)$, the viscous bending of the contact line will be small and hence the low resolution in our measurements is not going to affect the contact angle measurements substantially.

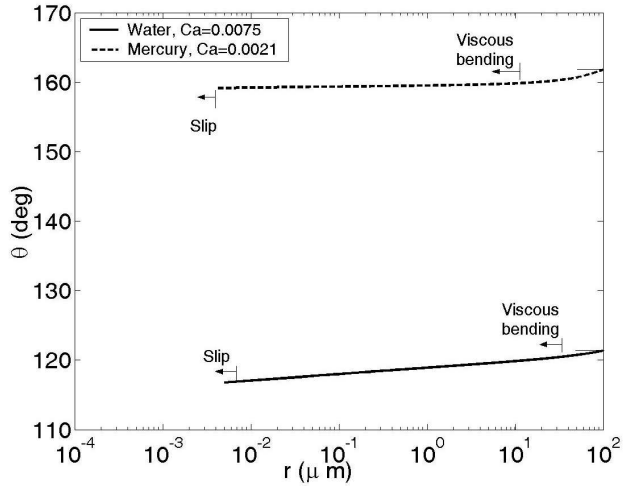

FIGURE 17. Variation of apparent contact angles with the resolution of measurement

Figure 17 shows the expected variation of the apparent contact angle with resolution, as calculated using the viscous bending relation given by Dussan *et al.* (1991).

$$g(\theta_d) = g(\theta_m) + Ca \ln(r/l_c) + g(f_o) \tag{A 1}$$

where, $g(\theta)$ is given by (4.10),

$$f_o = \frac{r}{l_c}\left[2S + \frac{l_c}{R_b}\left(\frac{2(C^3-1)}{3S} + \sin(\pi/2-\theta_m)\right)\right] - \frac{1}{2}\left(\frac{r}{l_c}\right)^2 \sin(\pi-\theta_m) \tag{A 2}$$

$$S = \sin(\pi/2-\theta_m)/2,\ C = \cos(\pi/2-\theta_m)/2 \tag{A 3}$$

θ_m is the microscopic contact angle, l_c is the capillary length and r the distance from the contact line at which the apparent contact angle is measured.

The variation shown in figure 17 is only approximate since we have used the expression for the interface in the outer region given by Dussan *et al.* (1991) for the case of immersing a tube into a layer of fluid. However the interface shape in the outer region should be similar to that in a sessile drop and hence the figure is indicative of the possible variation of the contact angle with the resolution. The curves shown in figure 17 are for water and mercury at the largest Ca encountered in our experiments. In obtaining these curves θ_m was adjusted so that θ_d at 100μm matched with the measured value at the corresponding Ca. Our measurements are at a resolution of 100μm. The figure shows that as we increase the resolution of measurement, viscous bending becomes predominant at about 10μm for mercury and at 35μm for water. Figure 17 shows that even if we were to measure the apparent contact angles at the boundary of outer region and the intermediate region, as is often suggested to be the best position, the maximum changes in the dynamic contact angles from the present values will be about 1.9° for mercury and 0.9° for water. These are the maximum possible changes at the highest Ca in our experiments that would be encountered if measurements are made with a resolution of 10μm in mercury and 35μm in water; the changes will be lower for most of our data that are at lower Ca. Considering that the variation in our repeated measurements itself is about 3°, such high resolution measurements are not going to change any of the results on dynamic contact angles that we have presented. The variation of θ_d due to improved resolution will be well within the error bar shown in figure 6. In addition, as part of an ongoing study, we have now conducted measurements at a higher resolution of 15 μm, but for different drop

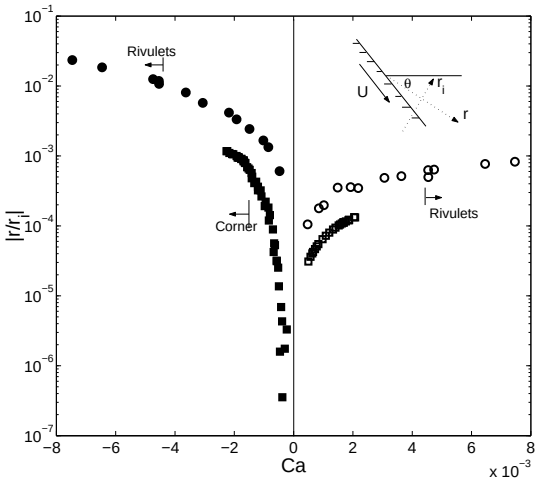

FIGURE 18. The ratio of radius of curvature of the interface to the distance from the triple point (B 1), as estimated from Huh & Scriven (1971) for the range of Ca and θ_d involved in the experiments. Filled symbols are for receding contact line and the open symbols for advancing contact line. ○, water; □, mercury.

diameters than that reported in the present paper. These measurements are consistent with the measurements presented in the paper.

Appendix B. Justification for using Huh & Scriven (1971) solution

The Huh & Scriven (1971) solution of creeping flow in a corner does not satisfy the normal stress boundary condition, as pointed out first by Huh & Scriven (1971) themselves. The solution is for a flat interface geometry, but the normal stress balance obtained from the solution will result in an equation for the curvature of the interface between a liquid and a gas of negligible viscosity as,

$$\frac{1}{r_i} = \frac{Ca}{r}\left(\frac{2\sin^2\theta_d + \sin 2\theta_d}{\sin 2\theta_d - \theta_d}\right). \tag{B 1}$$

This curvature has a singularity at $r = 0$, which is the crux of the contact line problem and is due to the conflicting boundary condition at the triple line, when approached from the solid-liquid interface and from the liquid-gas interface. In § 5.3, when the lubrication solution used in the de Gennes (1986) model is replaced by the Huh & Scriven (1971) solution, we truncate the solution at a slip length λ from the contact line, to avoid this singularity. This approach is similar to the approach followed in most slip models of dynamic contact angles.

The curvature of the interface $(1/r_i)$ when $r \neq 0$, is neglected in the Huh & Scriven (1971) solution. However, as is obvious from (B 1), this curvature tends to zero as $Ca \to 0$, when $r \neq 0$; the $r = 0$ case is anyway excluded by terminating the solution at the slip length. So Huh & Scriven (1971) solution will have a perfectly flat interface only when $Ca = 0$. However, for small Ca as in our experiments, the interface can be considered flat to first order, except at $r = 0$. The variation of the radius of curvature of the interface, normalised by the length scale r at which this curvature occurs is shown in figure 18 for the range of Ca in our experiments.

It is clear from the figure that even at the point of corner formation in mercury, the

radius of curvature of the interface at any $r \neq 0$ is four orders of magnitude larger than the value of r itself; the interface is for all practical purposes flat near the contact line. Of course this solution is valid only up to an r so that Re based on r is less than 1. So in effect the interface could be considered flat for $\lambda < r < \nu/U$. The variation of the length scale ν/U at which the local $Re \sim 1$ is shown in figure 7(a).

Appendix C. Estimate of ρ_G^s

Equation (4.12) is obtained after linearising the differential equations of interface formation under the assumption that the deviation of ρ_e^s from ρ_0^s is small, or in other words when $\rho_G^s \to 1$ so that the small parameter

$$(1 - \rho_G^s) \to 0. \tag{C 1}$$

The value of ρ_G^s hence has to be close to one as per the theory, usually between 0.9 and 0.99, but can never be equal to one. Equation (4.17) could be written as

$$(1 - \rho_G^s)\lambda = 1, \tag{C 2}$$

where $\lambda = \gamma\rho_0^s/\sigma_e$. One can find the value of ρ_G^s if the values of γ and ρ_0^s are known.

$$\rho_0^s \approx \rho\epsilon, \tag{C 3}$$

where we take $\epsilon = 3$nm for both water and mercury. The phenomenological coefficient γ in (4.17), reflects the ability of the interfacial layer to be rarefied or compressed due to the non-symmetric action of intermolecular forces from the bulk phases (Shikhmurzaev 2008). γ is inversely proportional to the compressibility of the fluid and its order is expected to be slightly less than the square of the speed of sound c for incompressible fluids (Shikhmurzaev 2008). The square of the speed of sound in water and in mercury are $c^2 = 2.2 \times 10^6$ m^2/s^2 and $c^2 = 2.1 \times 10^6$ m^2/s^2 respectively at 25°C (Everest 2001). Hence taking $\gamma < c^2$ and using (C 3), we get $\rho_G^s < 0.9891$ for water and $\rho_G^s < 0.9943$ for mercury from (C 2). We hence chose $\rho_G^s = 0.98$ for Si oil, water and mercury that will give values of γ slightly less than c^2 in all these fluids, at the same time ensuring that the condition (C 1) is met.

REFERENCES

Batchelor, G. K. 1969 *An introduction to fluid dynamics*. Cambridge University Press.

Bayer, I. S. & Megaridis, C. M. 2006 Contact angle dynamics in droplets impacting on flat surfaces with different wetting characteristics. *J. Fluid. Mech.* **558**, 415–449.

Ben Amar, M., Cummings, L. J. & Pomeau, Y. 2003 Transition of a moving contact line from smooth to angular. *Phys. Fluids* **15**, 2949–2960.

Bertozzi, A. L. & Brenner, M. P. 1997 Linear stability and transient growth in driven contact lines. *Phys. Fluids* **9**, 530.

Bikerman, J. J. 1950 Sliding of drops from surfaces of different roughnesses. *J. Colloid Sci.* **5**, 349.

Blake, T. D., Bracke, M. & Shikhmurzaev, Y. 1999 Experimental evidence of nonlocal hydrodynamic influence on the dynamic contact angle. *Phys. Fluids* **11** (8), 1995–2007.

Blake, T. D. & Haynes, J. M. 1969 Kinetics of liquid/liquid displacement. *J. Colloid Interface Sci.* **30**, 421–423.

Blake, T. D. & Ruschak, K. J. 1979 A maximal speed of wetting. *Nature* **489**, 489–491.

Bonn, D., Eggers, J., Indekeu, J., Meunier, J. & Rolley, E. 2009 Wetting and spreading. *Reviews of modern physics* **81**.

Cox, R. G. 1986 The dynamics of the spreading of liquids on a solid surface. *J. Fluid. Mech.* **168**, 169–194.

Cox, R. G. 1998 Inertial and viscous effects on dynamic contact angles. *J. Fluid. Mech.* **357**, 249–278.

Durbin, P. A. 1988 Considerations on the moving contact-line singularity, with application to frictional drag on a slender drop. *J. Fluid. Mech.* **197**, 157–169.

Dussan, V. E. B. 1979 On the spreading of liquids on solid surfaces: static and dynamic contact lines. *Annu. Rev. Fluid Mech.* **11**, 371400.

Dussan, V. E. B. 1985 On the ability of drops or bubbles to stick to non-horizontal surfaces of solids, part 2: small drops or bubbles having contact angles of arbitrary size. *J. Fluid. Mech.* **151**, 1–20.

Dussan, V. E. B. & Chow, R. T. P. 1983 On the ability of drops or bubbles to stick to non-horizontal surfaces of solids. *J. Fluid. Mech.* **137**, 1–29.

Dussan, V. E. B. & Davis, S. H. 1974 On the motion of a fluid-fluid interface along a solid surface. *J. Fluid. Mech.* **65**, 71–95.

Dussan, V. E. B., Rame, E. & Garoff, S. 1991 On identifying the appropriate conditions at a moving contact line : an experimental investigation. *J. Fluid. Mech.* **230**, 97–116.

Eggers, J. 2004 Toward a description of contact line motion at higher capillary numbers. *Phys. Fluids* **16** (9).

Eggers, J. & Evans, R. 2004 Comment on 'Dynamic wetting by liquids of different viscosity' by T. D. Blake and Y. D. Shikhmurzaev. *Jl. of Colloids and Interface Science* **280**, 537–538.

Everest, F. 2001 *The master handbook of acoustics*, 4th edn. McGrawhill NewYork.

Furmidge, C. G. L. 1962 Studies at phase interfaces. i. the sliding of liquid drops on solid surfaces and a theory for spray retention. *J. Colloid Sci.* **17**, 379.

de Gennes, P., Brochard-Wyart, F. & Quere, D. 2004 *Capillarity and wetting phenomena: drops, bubbles, pearls, waves*. Springer.

de Gennes, P. G. 1986 Wetting: statics and dynamics. *Rev. of Modern Physics* **3**, 57.

Gupta, P. K., Inniss, D., Kurkjian, C. R. & Zhong, Q. 2000 Nanoscale roughness of oxide glass surfaces. *Jl. non-crystalline solids* **262** (1-3), 200–206.

Hayes, R. A. & Ralston, J. 1993 Forced liquid movement on low energy surfaces. *J. Colloid Interface Sci.* **159**, 429–438.

Henderson, J. R. 2011 Discussion notes on "Some dry facts about dynamic wetting", by Y.D.Shikhmurzaev. *Eur. Phys. J. Special Topics* **197**, 61–62.

Holleman, A. F. & Wiberg, E. 2001 *Inorganic Chemistry*. Academic Press, SanDiego.

Hozumi, A., Ushiyama, K., Sugimura, H. & Takai, O. 1999 Fluoroalkylsilane monolayers formed by chemical vapor surface modification on hydroxylated oxide surfaces. *Langmuir* **15**, 7600–7604.

Huh, C. & Scriven, L. E. 1971 Hydrodynamic model of steady movement of a solid/liquid/fluid contact line. *J. Colloid Interface Sci.* **35**, 85.

Jerrett, J. M. & de Bruyn, J. R. 1992 Fingering instability of a gravitationally driven contact line. *Physics of Fluid A* **4**, 234.

Kim, H. Y., Lee, H. J. & Kang, B. H. 2002 Sliding of liquid drops down an inclined solid surface. *J. Colloid Interface Sci.* **247**, 372–380.

Lamb, H. 1932 *Hydrodynamics*, chap. 5, p. 586. Cambridge Univ. Press.

Le Grand, N., Daerr, A. & Limat, L. 2005 Shape and motion of drops sliding down an inclined plane. *J. Fluid. Mech.* **541**, 293–315.

Limat, L. & Stone, H. A. 2004 Three dimensional lubrication model of a contact line corner singularity. *Europhys. Lett.* **65**, 365.

Lopez, P. G., Bankoff, S. G. & Miksis, M. J. 1996 Non-isothermal spreading of a thin liquid film on an inclined plane. *J. Fluid. Mech.* **324**, 261–286.

Lopez, P. G., Miksis, M. J. & Bankoff, S. G. 1997 Inertial effects on contact line instability in the coating of a dry inclined plate. *Phys. Fluids* **9**, 2177.

Mahadevan, L. & Pomeau, Y. 1999 Rolling droplets. *Phys. Fluids* **11**, 2449–2452.

Petrov, J. G., Ralston, J., Schneemilch, M. & Hayes, R. A. 2003 Dynamics of partial wetting and dewetting in well-defined systems. *J. Phys. Chem* **107** (7), 1634.

Petrov, J. G. & Sedev, R. V. 1992 A combined molecular-hydrodynamic approach to wetting kinetics. *Langmuir* **19**, 1762.

Pismen, L. 2011 Discussion notes on "Some dry facts about dynamic wetting", by Y.D.Shikhmurzaev. *Eur. Phys. J. Special Topics* **197**, 63–65.

Podgorski, T., Flesselles, J. M. & Limat, L. 2001 Corners, cusps and pearls in running drops. *Phys. Fluids* **87**, 036102.

Prabhala, B. R., Panchagnula, M. V. & Vedantam, S. 2012 Three dimensional equilibrium shapes of drops on hysteretic surfaces. *Colloid and Polym Sci* **DOI 10.1007/s00396-012-2774-z**.

Richard, D. & Quéré, D. 1999 Viscous drops rolling on a tilted non-wettable solid. *Europhys. Lett.* **3**, 286–291.

Rio, E., Daerr, A., Andreotti, B. & Limat, L. 2005 Boundary conditions in the vicinity of a dynamic contact line: Experimental investigation of viscous drops sliding down an inclined plane. *Phys. Rev. Lett.* **94** (2), 024503.

Rolley, E. & Guthmann, C. 2007 Dynamics and hysteresis of the contact line between liquid hydrogen and cesium substrates. *Phys. Rev. Lett.* **98**, 166105.

Seveno, D., Vaillant, R. R., Adao, H., Conti, J. & DeConinck, J. 2009 Dynamics of wetting revisited. *Langmuir* **25** (22), 13034–13044.

Shikhmurzaev, Y. 2011*a* Discussion notes on "Disjoining pressure of planar adsorbed films", by J.R.Henderson. *Eur. Phys. J. Special Topics* **197**, 125–127.

Shikhmurzaev, Y. 2011*b* Discussion notes on "Some singular errors near the contact line singularity, and ways to resolve both", by L.M.Pismen. *Eur. Phys. J. Special Topics* **197**, 75–80.

Shikhmurzaev, Y. 2011*c* Some dry facts about dynamic wetting. *Eur. Phys. J. Special Topics* **197**, 47–60.

Shikhmurzaev, Y. D. 1993 The moving contact line on a smooth solid surface. *Int. J. Multiphase Flow* **19(4)**, 589–610.

Shikhmurzaev, Y. D. 2008 *Capillary flows with forming interfaces*. Chapman and Hall/CRC.

Shikhmurzaev, Y. D. & Blake, T. 2004 Response to the comment on [Jl. Colloid and Interface Science. 253,(2003), 196] by Eggers. J and Evans R. *Jl. of Colloids and Interface Science* **280**, 539–541.

Snoeijer, J. H., Le Grand, N., Limat, L., Stone, H. A. & Eggers, J. 2007 Cornered drops and rivulets. *Phys. Fluids* **19**, 042104.

Snoeijer, J. H., Rio, E., Le Grand, N. & Limat, L. 2005 Self-similar flow and contact line geometry at the rear of cornered drops. *Phys. Fluids* **17**, 072101.

Thiele, U. 2011 Discussion notes: Thoughts on mesoscopic continuum models. *Eur. Phys. J. Special Topics* **197**, 67–71.

Troian, S. M., Herbolzheimer, E., Safran, S. A. & Joanny, J. F. 1989 Fingering lnstabilities of driven spreading films,. *Europhysics letters* **10**, 25.

Voinov, O. V. 1976 Hydrodynamics of wetting. *Fluid Dyn.* **11**, 714721.

Winkels, K. G., Peters, I. R., Evangelista, F., Riepen, M., Daerr, A., Limat, L. & Snoeijer, J. H. 2011 Receding contact lines: from sliding drops to immersion lithography. *The Euro. Jl. of Phys.* **192**, 195–205.